THREE-DIMENSIONAL INDETERMINATE IMPACTS IN LEGGED ROBOTIC LOCOMOTION

by

ABHISHEK CHATTERJEE

Presented to the Faculty of the Graduate School of
The University of Texas at Arlington in Partial Fulfillment
of the Requirements
for the Degree of

MASTER OF SCIENCE IN MECHANICAL ENGINEERING

THE UNIVERSITY OF TEXAS AT ARLINGTON

May 2015

To my parents, Alokananda and Asoke Chatterjee, whose guidance and support made me who I am.

ACKNOWLEDGEMENTS

I would like to thank my supervising professor Dr. Alan Bowling for constantly motivating and encouraging me, and also for his invaluable advice during the course of my graduate study. I wish to thank Dr. Ashfaq Adnan and Dr. Kamesh Subbarao for their interest in my research and for taking time to serve in my thesis committee.

I would like to thank all my current and past friends and colleagues from The Robotics, Biomechanics and Dynamic Systems Lab. Dr. Adrian Rodriguez and Dr. Mahdi Haghshenas-Jaryani for their patient guidance and support during my initial days in the lab. Ashley Chase Guy, Yatish Nagraj, Rohit Katti, Pranav Parikh and Nachiket Kansara for all their support and valuable feedback regarding my work and also for being good companions in the lab. I would like acknowledge my friend Philip Bailey, who once helped me identify a bug in one of the codes that I had written for my research.

I would like to express my deepest gratitude to my mother, Alokananda Chatterjee and father Asoke Chatterjee, without whose support and sacrifices, it would have been impossible for me to continue chasing my long-term dream of becoming a robotics researcher. I would like to thank my old friend Sajjad Pathan, whose guidance and moral support made a lot of difference, when I was an inexperienced college freshman, living far away from home in a foreign country. I wish to thank all my undergraduate professors, especially Dr. Salim Azzoz who mentored me during my undergraduate research and Dr. Dale McDonald who sparked in me the interest for

Dynamics and Controls. Finally, I would also like to thanks my friends and companions Jaganmohan Chandrasekaran and Danny John, for all the moral support they provided during the tough patches of my journey through graduate school.

April 22, 2015

ABSTRACT

THREE-DIMENSIONAL INDETERMINATE IMPACTS IN
LEGGED ROBOTIC LOCOMOTION

ABHISHEK CHATTERJEE, M.S.

The University of Texas at Arlington, 2015

Supervising Professor: Alan P. Bowling

Legged robotic systems undergo a large number of impacts during walking or running tasks. These impacts occur over the surface of contact between the feet and the ground. If a rigid body assumption is held, these impacts can be analyzed by selecting a certain number of points on the impacting bodies. A minimum of three points are required for analyzing a surface contact on a plane. However, using a minimum number of points for analyzing surface impact would require an additional analysis for appropriately selecting these points. On the other hand, if a large number of evenly distributed impact points are used for the analysis, there wouldn't be a need for this additional analysis. However, as more and more impact points are added, the impact analysis problem can become indeterminate if the number of constraint forces exceed the number of degrees of freedom of the system.

This work provides a framework for the analysis of indeterminate impacts while using a large number impact points on the surface of the foot. A comparison is presented in this work between the results obtained by selecting varying number

of points for impact analysis. This essentially shows that post-impact behavior of the impacting bodies are independent of the number of points used for the impact analysis. Finally, this framework has also been implemented in a model of a bipedal robotic system undergoing a walking task.

TABLE OF CONTENTS

Appendix

LIST OF ILLUSTRATIONS

CHAPTER 1

INTRODUCTION

In the past few decades, legged robotic systems have been of great interest in the robotic research community. One characteristic of legged systems such as bipeds or quadrupeds is that these are floating base systems, and have no fixed point in the environment. The position and orientation of the base of such a system is described with the six degrees-of-freedom in reference to the inertial frame. These floating base system, having no actuators to directly control the positions and orientations of the base, can be classified as an under-actuated robotic system. Thus, the generalized coordinates associated with the floating base needs to be controlled based on the other actuators in the system. Legged robots constantly interact with the ground such that the contact constraint forces on the feet of a robot behave as additional actuators, and indirectly contribute to the control of the position and orientation of the base. These contact constraint forces become impulsive during walking or running tasks or whenever the feet surface gets into contact with some amount of velocity. In such situations, the feet are said to be undergoing impact. Surface contact lasts for a very small period of time during impacts, and the constraint forces become very large, resulting in an instantaneous change in velocity.

Impacts on surfaces, such as the once that take place between the robot feet and the ground, can be analyzed by considering a number of distinct points on the contact surface. Then the post-impact behavior of the entire surface can be characterized based on the impact analysis. Three different points are necessary to represent a flat surface. However, if three points are to be selected for the analysis, an additional

analysis is required to appropriately select these three points. These points need to be selected based on the geometry of the impacting body, assuming a perfectly flat(plane) ground. Based on how these points are selected, a center of pressure is created for the impact, thus giving a direction to the ground reaction force vector. In order to accurately analyze an impacting surface, the three points for analysis are required to be chosen in such a way that ground reaction force through the center of pressure is always normal to plane of impact [1]. In case, that the ground isn't perfectly flat, a further analysis is needed to identify the plane of impact. Therefore, given these drawbacks related to the selection of the minimum three points to characterize the surface impacts, a better solution to the problem would be to extend the analysis to a greater number of evenly distributed points on the surface.

Analysis of a surface impact using a given number of contact points for analysis, is performed based on the equations of motion for the system. The contact constraint forces are represented in the equations of motion, in terms of the generalized forces such that each contact point contributes three constraint force components. Thus, increasing the number of analysis points effectively means increasing the number constraint force component terms in the equations of motion. The goal of the impact analysis is to solve for these constraint forces such that the post-impact velocities for the impacting bodies can be resolved based on these forces. However, when the number of analysis points are increased such that the number of constraint forces exceed the number of degrees of freedom in the system, the impact analysis becomes an indeterminate problem, as the number of unknowns in the system exceeds the number of equations available to solve. Thus, addressing this indeterminacy becomes crucial to extending the number of impact analysis points on the surface of contact.

Many different approaches for analyzing indeterminate impacts can be found in the literature. One class of methods address the indeterminacy by adding more

degrees-of-freedom (DOFs) to the problem. This increases the number of equations available to solve for the extra forces. These approaches may be grouped together into the class of *continuous* or *compliant* methods where material deformations due to the impac are taken into account [2, 3, 4]. In this work hard impacts are considered where there is negligible deformation of the colliding bodies. Hard impacts exhibit a sudden jump in the velocities of the contact points when examined over a larger time scale, which appears to be a discontinuity in the velocities. This situation is modeled better using a discrete approach.

The discrete approach is commonly obtained by integrating the equations of motion over an infinitesimally small time period as is done in classical impulse-momentum theory. Because of the small time period, it is assumed that the configuration does not change significantly during the collision [5, 6, 7]. The goal is to find the post-impact velocities given the system's pre-impact velocities. There are two main discrete approaches, classified as *analytic* or *iterative methods*. The iterative methods establish an optimization problem, which searches for a solution by minimizing a cost function using standard optimization techniques. This includes penalty methods, lagrange multiplier approaches, and energy dissipation principles [8, 9, 10, 11]. Analytic methods use algebraic impulse-velocity relationship and predicts the post-impact velocities based on parameters such as coefficients of friction and restitution[12, 13, 14].

For planar two-dimensional problems, there exists no impact-plane and consequently the slip direction is not taken into account, thus the differential equations describing the impact state could be converted into simple algebraic equations in terms of the normal impulses, which could be solved analytically[12, 13, 14]. Nevertheless, such an analytical framework doesn't prove to be useful for three-dimensional indeterminate impact problems, with the exception of a certain limited set of impact

configurations (i.e. collinear/central). Complications arise when friction is modelled due to the non-linearities associated with sliding friction on the slip plane of the impact point. This further leads to five first-order non-linear ordinary differential equations in the case of single point impact [15, 16, 17, 18, 19, 20]. The problem that arises in 3D impact problems with friction is determining the slip direction θ of the impact after it comes to rest. Note that the slip direction is a result of the the two tangential velocity components of the sliding point on the slip plane. Stronge showed that for collinear or central collision of bodies that are axisymmetric about the common normal direction, the direction of slip θ does not vary [15]. Bhatt et. al qualitatively classified different sliding behavior using impact induced flow in tangent velocity space, on the basis of certain invariant and flow change directions that were found through the analysis[21].

The primary goal of this work is to develop a framework to analyze rigid impacts using a large number of analysis points in legged robotic systems. This work describes a general method for modeling indeterminate impacts using the equations of motion. This method can be applied to different kinds of legged systems, with appropriate adjustments. In this work it is also shown that if more number of evenly distributed points are selected for the analysis of impacts, there is no difference in the post impact behavior as compared to the case where a minimum set of points are appropriately selected. This would relieve the need for the additional analysis based on the center of pressure the selection of the points, because with large number of evenly distributed points on the contact surface, the ground reaction force would always remain normal to the impact plane.

In chapter 2 a detailed discussion is presented on the methods used for modeling three-dimensional, frictional multiple point contacts and impacts. The method presented in this section relies on a modified version of the equations of motion that

relates the contact constrained velocities with respect to impulses that occur over very small period of time. Chapter 3 presents some results on an impacting block, using the impact analysis methods detailed in chapter 2. Following the details of the impact analysis method, a few results of impact analysis on a walking bipedal robotic system are presented. A model of the ATLAS robot is used to demonstrate the application of impact analysis on legged robotic system. In chapter 4 a discussion is presented on the methodology used for controlling the bipedal system. Chapter 5 discusses the results obtained by implementing the impact model on a bipedel robotic system.

CHAPTER 2

IMPACT MODEL

2.1 Model Description

This section would describe the various parameters that would be used through out this chapter. The method described in the following sections are very general in nature and can be applied for different kinds of systems that share certain features with the bipedal system.

Let, there be an inertial reference frame $\mathbf{N} \in \mathbb{R}^{\mathbf{3}}$ with the basis $\hat{\mathbf{N}}_{\mathbf{1}} = [1, 0, 0]^T$, $\hat{\mathbf{N}}_{\mathbf{2}} = [0, 1, 0]^T$ and $\hat{\mathbf{N}}_{\mathbf{3}} = [0, 0, 1]^T$. Then a robot of N_d degrees-of-freedom can be described using a set of generalized coordinates $\mathbf{q} \in \mathbb{R}^{N_d}$ such that,

$$\mathbf{q} = [q_1, q_2, ..., q_{N_d}]^T \tag{2.1}$$

where $q_1, ...q_{N_d}$ are the coordinates that can completely describe the positions and orientation of the robotic system. These coordinates are composed of the position and orientation components of the free floating base and the various joint angles in the system. The number of bodies experiencing impact at any given instant is N_b. Let the number of contact point considered on a body i be n_i, where $i = 1, .., N_b$. Therefore, the total number of contact points and constraint forces on the system would be $N_p = \sum_{i=1}^{N_b} n_i$ and $N_c = 3 \sum_{i=1}^{N_b} n_i$, respectively. The number of actuator torques in the system is given by N_t.

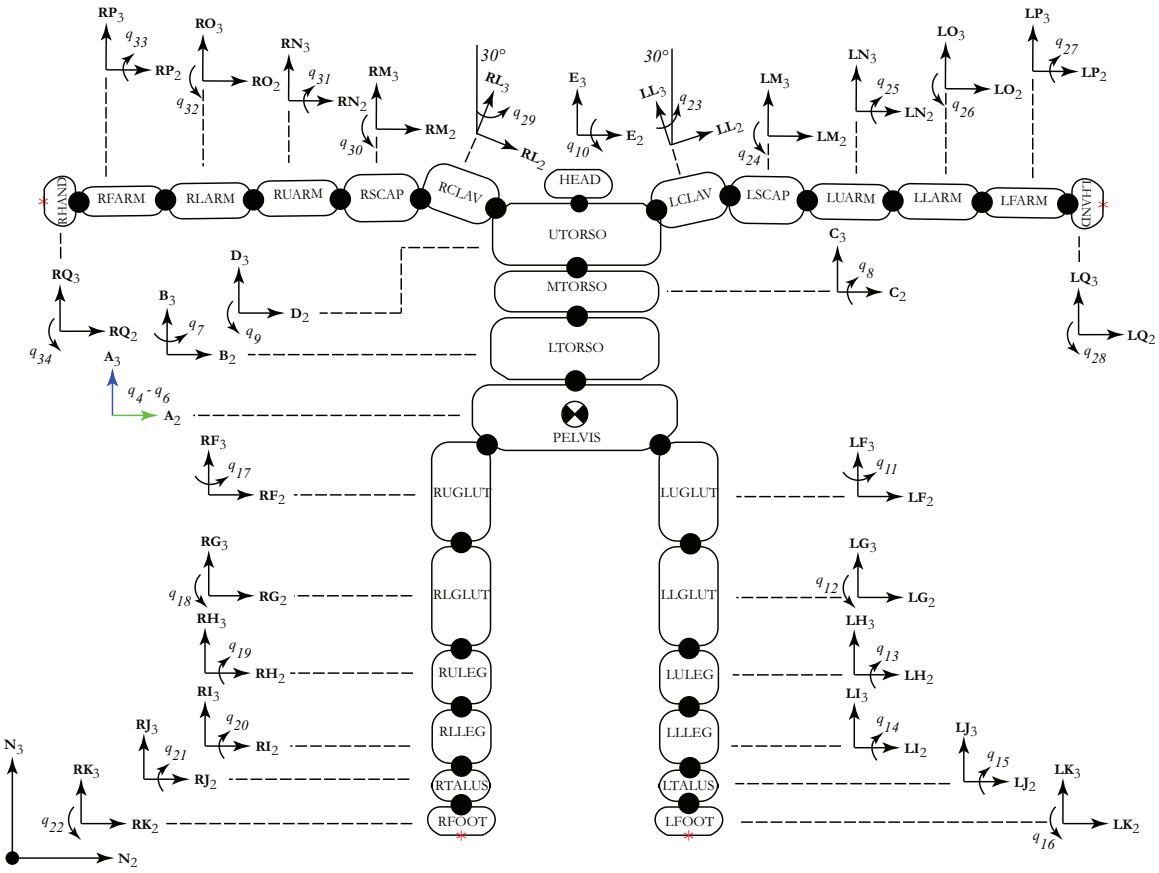

Figure 2.1. Degrees of freedom.

2.2 Equations of Motion

Based on the model parameters described in the previous section an equations of motion for the robotic system can be written without any loss of generality,

$$A\,\ddot{\mathbf{q}} \;+\; \mathbf{b}(\mathbf{q},\dot{\mathbf{q}}) \;+\; \mathbf{g}(\mathbf{q}) \;= J_c{}^T\,\mathbf{F} \;+ G^T\boldsymbol{\Gamma} \tag{2.2}$$

where,

$$\mathbf{F} = [f_1, f_2, ..., f_{N_c}]^T$$

$$\boldsymbol{\Gamma} = [\Gamma_1, \Gamma_2, ..., \Gamma_{N_t}]^T$$

$$A \in \mathbb{R}^{N_d \times N_d}$$

$$\mathbf{b} \in \mathbb{R}^{N_d}$$

$$\mathbf{g} \in \mathbb{N}$$

$$J_c \in \mathbb{R}^{N_c \times N_d}$$

$$G \in \mathbb{R}^{N_t \times N_d}$$

In equation(2.2) A is the inertia matrix, while $\mathbf{b}$ and $\mathbf{g}$ are vectors containing the coriolis and gravity terms respectively. $\mathbf{F}$ is a vector containing all the constraint forces acting on the system. J_c is a jacobian matrix containing row vectors corresponding to each coordinate of the contact points. $\mathbf{\Gamma}$ is a vector containing all the actuator torques in the system, and G is a permutation matrix that selects the appropriate torques corresponding to each actuated degree of freedom.

2.3 Impact Law

In this and the following section, the equations of motion, as described in (2.2) would be used to formulate an impact law for resolving the contact constraints during an impact event. This impact law can be used to analyze impacts that causes the system to rebound as well as stable contacts. Contacts are considered to be successive impacts with diminishing energy loss. This recursion is terminated when the energy loss due to an impact is very close to zero, or the post-impact velocities of the contact points within a threshold range.

Mechanical systems when subjected to an impact, experience an instantaneous change in its velocities. These instantaneous changes of velocities are a result of the energy loses endured by the system due to friction and infinitesimally small material deformations around the contact region. In this model small scale deformations of the bodies are going to be ignored, thus maintaining a rigid body assumption. Another assumption made in this work is that there is no change in the configuration of the

entire system during an event, or in other words the generalized coordinates, $\mathbf{q}$ of the system remain constant during the impact event. This assumption follows from the fact that there instantaneous change in velocity and due to the infinitesimally small time-period of impact the change in positions of the system can be considered negligible.

As the robotic system experiences impact there is an instantaneous change in the velocities of the system, which gives rise to apparent discontinuities in the state trajectories, on a large time-scale. However, over the infinitesimally small time-period of the impact event, the state trajectories are continuous. Hence the equations of motion are integrable during the impact event. Thus, performing an integration over a small period ϵ gives,

$$\int_t^{t+\epsilon} [A\ \ddot{\mathbf{q}}\ +\ \mathbf{b}(\mathbf{q},\dot{\mathbf{q}})\ +\ \mathbf{g}(\mathbf{q})\ ]\ dt = \int_t^{t+\epsilon} \left[{J_c}^T\ \mathbf{F}\ + G^T\mathbf{\Gamma}\right]\ dt \tag{2.3}$$

As a result of the assumptions previously stated, the generalized coordinates, $\mathbf{q}$ remains constant. The instantaneous change in velocities of the contact points result in a finite amount of change in generalized velocities, $\dot{\mathbf{q}}$. However, this also implies that the change in generalized accelerations $\ddot{\mathbf{q}}$ and constraint forces $\mathbf{F}$ would tend towards infinitesimally large values. In (2.3), the jacobian and inertia matrices are functions of $\mathbf{q}$, and consequently would remain constant during the impact event. Similarly, the gravity terms being a function of $\mathbf{q}$ would remain constant during the impact. The coriolis terms and the actuator torques would have a finite amount of change during the impact event. However, since the time period ϵ over which the integration is being performed is infinitesimally small, all the integrands that have a bounded or finite magnitude would yield negligible results upon integration, whereas all inte-

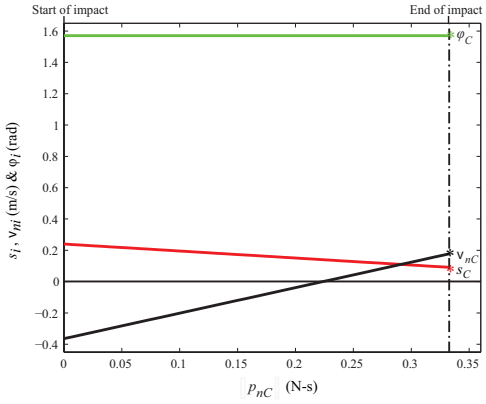

Figure 2.2. Typical Velocity Plot during Impact Event.

grands tending towards infinitesimally large magnitudes would yield finite/bounded results upon integration. Therefore,

$$\lim_{\epsilon\to\infty}\int_t^{t+\epsilon}\mathbf{b}(\mathbf{q},\dot{\mathbf{q}})dt \approx \mathbf{0}$$

$$\lim_{\epsilon\to\infty}\int_t^{t+\epsilon}\mathbf{g}(\mathbf{q})dt \approx \mathbf{0}$$

$$\lim_{\epsilon\to\infty}\int_t^{t+\epsilon}G^T\mathbf{\Gamma}dt \approx \mathbf{0}$$

Hence the equation (2.3) can be reduced to,

$$A\int_t^{t+\epsilon}\ddot{\mathbf{q}}dt = {J_c}^T\int_t^{t+\epsilon}\mathbf{F}dt \tag{2.4}$$

After performing the integration, the above equation can be written in terms of the velocities of the contact points,

$$\boldsymbol{\vartheta} \ -\boldsymbol{\vartheta}_o = \boldsymbol{\vartheta}(t+\epsilon) \ - \ \boldsymbol{\vartheta}(t) \ = \ \underbrace{J_c A^{-1} {J_c}^T}_{M}\ \mathbf{p} \tag{2.5}$$

Where $\boldsymbol{\vartheta}_o$ and $\boldsymbol{\vartheta}$ are the pre- and post-impact velocities of the contact point, respectively. $\mathbf{p}$ is the vector containing all the impact impulses during the impact event. The goal is to find the impulses, $\mathbf{p}$ for a given impact, such that post-impact velocities could be calculated, and subsequently the integration could be restarted using

these post-impact velocities as initial condition. Now, the $\mathbf{p}$ needs to be such that the impact is energetically consistent. In order to find the impulses such that the system is energetically consistent, the first step would be to reduce the equation (2.3) in terms of one independent variable. Figure (2.3) is taken from [1], shows velocities of impact points evolving on the basis of one independent impulse. The following two sections are going to discuss that process.

2.4 Coulomb's Law of Friction

During an impact event, in addition to the normal forces, tangential forces along the impact plane are also applied on the system. These tangential forces arise due to the friction between the contact point and the surface. The tangential frictional forces acting on the system can be described in terms of the Amonton-Coulomb's law of friction in $\mathbb{R}^3$ given by,

$$\|\mathbf{f_t}\| \leq \mu f_n \tag{2.6}$$

where, $\mathbf{f_t} = [f_{t1}, f_{t2}]^T$ is a vector containing the frictional force acting tangential to the impact plane, such that f_{t1} and f_{t2} are the components of the frictional force in the two tangential directions. μ is the coefficient of limiting(sliding) friction and f_n is the normal force acting on the impact plane.

This work deals with the coulomb's friction that is applied to various contact points of the bodies. Therefore, the coulomb's law expressed in (2.6) needs to be extended for multiple point contact and impact. As opposed to (2.6) which is in $\mathbb{R}^3$, the coulomb's law for multiple-point friction needs to be defined in $\mathbb{R}^{N_c}$. The constraint force vector defined in section 2.2 can be written as,

$$\mathbf{F} = [f_k]_{N_c \times 1}$$

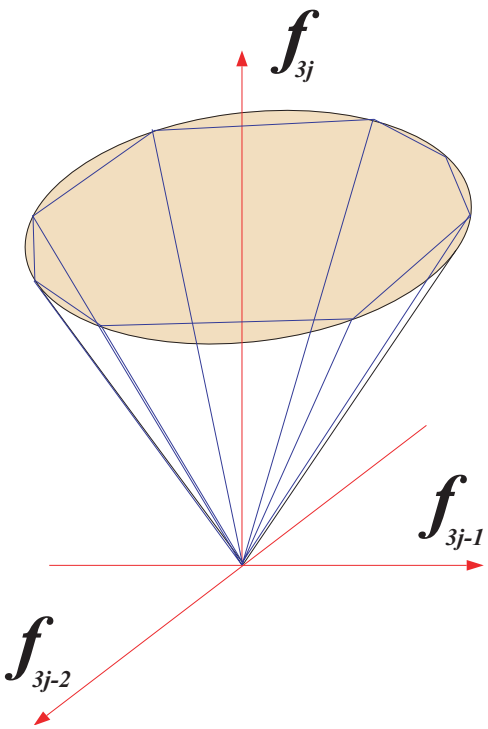

Figure 2.3. Friction Cone.

Such that $k = 1, .., N_c$. $\mathbf{F}$ is a concatenation of smaller three-element force vectors associated with each point on the impacting bodies, such that the first and second elements of these smaller vectors represent the tangential components whereas the element represents the normal component of the point force. Thus, the frictional force terms in $\mathbf{F}$ can be describe using (2.6) as,

$$\sqrt{{f_{3j-2}}^2 + {f_{3j-1}}^2} \leq \mu_j f_{3j} \quad \text{for} \quad j = 1, .., N_p \tag{2.7}$$

Where, N_p is the total number of contact points for the entire system, μ_j is the coefficient of friction for the j^{th} point. The coulomb's law stated in (2.6) and (2.7) is a discontinuous law of friction. The inequality in the equation accounts for the fact that the magnitude of the maximum frictional force that can act upon a body during sliding, and is given by $\mu_j f_{3j}$. The body sticks whenever the magnitude of the frictional force is less than $\mu_j f_{3j}$. The development that follows in the current

and the following section, would consider all frictional forces to be arising due to sliding friction. In section 2.7, a discussion is provided about the incorporation of sticking phenomenon in coulomb's law. Thus, when we consider only sliding friction the inequality in (2.6) is replaced by an equality, and the frictional force can be broken into the two planar components,

$$f_{3j-2} = -\mu_j \cos\phi_j f_{3j} \qquad\qquad f_{3j-1} = -\mu_j \sin\phi_j f_{3j} \tag{2.8}$$

where, ϕ_j represents the sliding angle on the slip plane. Note, that the each component of force on the tangent plane has a negative sign. This is because frictional force always acts in a direction opposite to the direction of slip. The direction of slip for a given point is a function of the velocities of the point. Therefore, given the velocities of a point $\boldsymbol{\vartheta} = [\vartheta_k]_{N_c \times 1}$, expressions for $\sin\phi_j$ and $\cos\phi_j$ for $j = 1, .., N_p$, can be written as,

$$\cos\phi_j = \frac{\vartheta_{3j-2}}{\sqrt{{\vartheta_{3j-2}}^2 + \vartheta_{3j-1}^2}} \qquad\qquad \sin\phi_j = \frac{\vartheta_{3j-1}}{\sqrt{{\vartheta_{3j-2}}^2 + \vartheta_{3j-1}^2}}$$

From the equation (2.8),

$$\frac{dp_{3j-2}}{dt} = -\mu_j \cos\phi_j \frac{dp_{3j}}{dt} \qquad\qquad \frac{dp_{3j-1}}{dt} = -\mu_j \sin\phi_j \frac{dp_{3j}}{dt} \tag{2.9}$$

Performing an integration would yield,

$$p_{3j-2} = -\mu_j \int \cos\phi_j dp_{3j} \qquad\qquad p_{3j-1} = -\mu_j \int \sin\phi_j dp_{3j} \tag{2.10}$$

Therefore, the impulse vector $\mathbf{p} = [p_k]_{N_c \times 1}$ can be substituted in (2.5). However, since the tangential impulses can be related to the normal impulses, as shown in equation (2.10), the velocities of the contact point can be defined as,

$$\boldsymbol{\vartheta} \ - \boldsymbol{\vartheta}_o = M \int H d\mathbf{p}_n \tag{2.11}$$

where, H is a transformation matrix that applies Coulomb's law on N_p contact points and is given by,

$$H = [h_{k,j}]_{N_c \times N_p} \text{ s.t. } h_{kj} = \begin{cases} -\mu_j \cos\phi_j & \text{if} \quad k = 3j-2 \\ -\mu_j \sin\phi_j & \text{if} \quad k = 3j-1 \\ 1 & \text{if} \quad k = 3j \\ 0 & \text{if} \quad 3j-2 > k > 3j \end{cases}$$

and $d\mathbf{p}_n$ is a vector containing the normal components of the differential impulses,

$$d\mathbf{p}_n = [dp_{nj}]_{N_p \times 1}$$

Where $k = 1, .., N_c$ and $j = 1, .., N_p$, and dp_{nj} corresponds to the normal impulses of each contact point. Equation (2.11) shows the numerical integration required to compute the velocities during the impact event. In order to perform the numerical integration with appropriate initial conditions the same equation needs to be rewritten in a differential form,

$$d\boldsymbol{\vartheta} = MHd\mathbf{p}_n \tag{2.12}$$

Note that the matrices M, which describes the inertia and configuration properties of the system and H, which describes the tangential forces in terms of the normal forces, remain constant during the impact event. Next step would be to describe the equation (2.12) in terms of one independent normal impulse.

2.5 Rigid Body Constraint

So far in this analysis, the number of independent variables have been reduced by relating the tangential differential impulses to the normal differential impulses using coulomb's law of friction. In this section, all the differential normal impulses would

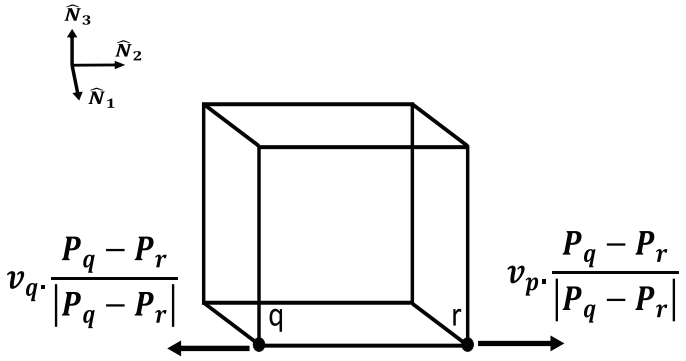

Figure 2.4. Relative Velocities of Different Points on a Rigid Body.

be constrained in terms of one independent differential normal impulse. Reducing all the contact point differential impulses in the system in terms of one independent differential normal impulse would help determine the end of the compression phase of the impact through an estimation of the energy loss in the system.

In [12], the application of the velocity constraints at the force level were derived using the dual properties of the impact Jacobian. Here, the constraints are found in differential form to be consistent with the remainder of the numerical framework.

Consider, the system where N_b number of bodies are undergoing impact. Within an impacting body i, such that $i = 1, .., N_b$ any two impact points be q and r, such that $q, r = 1, .., n_i$. The body is considered to be non-deformable, due to the rigid body assumption. Therefore, the relative-velocity component along the direction through the points q and r must be zero. Let the velocity vector for the impact points, $\boldsymbol{\vartheta}$ be rewritten as a concatenation of smaller vectors $\mathbf{V_i}$ representing the velocity vector for each point within a body,

$$\boldsymbol{\vartheta} = \left[\mathbf{V_1}^T, ..., \mathbf{V_{N_b}}^T\right]^T$$

And,

$$\mathbf{V}_i = \left[\mathbf{v}_1{}^T, ..., \mathbf{v}_{n_i}{}^T\right]^T$$

where, $\mathbf{v}_q$ for $q = 1, .., n_i$ are smaller three-dimensional vectors containing the velocity components of the each contact point in a body i, that consists of n_i contact points.

Then the relationships for the rigid body constraints between each point can be written as,

$$(\mathbf{v}_q - \mathbf{v}_r) \cdot \frac{\mathbf{P}_q - \mathbf{P}_r}{|\mathbf{P}_q - \mathbf{P}_r|} \;=\; 0 \quad \text{for} \quad \begin{matrix} q, r = 1, ...n_i \\ q \neq r \end{matrix} \tag{2.13}$$

Where, and the $\mathbf{P}_q$ and $\mathbf{P}_r$ are the position vectors (not to be confused with the impulse vectors) of the corresponding contact points with respect to some body attached reference point. The equation (2.13) can be expanded in terms of the inertial reference frame as follows,

$$\begin{aligned} &\Big[(v_{t1q}\hat{\mathbf{N}}_\mathbf{1} + v_{t2q}\hat{\mathbf{N}}_\mathbf{2} + v_{nq}\hat{\mathbf{N}}_\mathbf{3}) - (v_{t1r}\hat{\mathbf{N}}_\mathbf{1} + v_{t2r}\hat{\mathbf{N}}_\mathbf{2} + v_{nr}\hat{\mathbf{N}}_\mathbf{3})\Big] \\ &\qquad \cdot \Big[X_{qr}\hat{\mathbf{N}}_\mathbf{1} + Y_{qr}\hat{\mathbf{N}}_\mathbf{2} + Z_{qr}\hat{\mathbf{N}}_\mathbf{3}\Big] = 0 \end{aligned} \tag{2.14}$$

where X_{qr}, Y_{qr} and Z_{qr} are the direction cosines of the position vector $\mathbf{P}_{qr} = \mathbf{P}_q - \mathbf{P}_r$.

$$(v_{t1q} - v_{t2r})X_{qr} \;+\; (v_{t2q} - v_{t2r})Y_{qr} + \; (v_{nA} - v_{nB})Z_{qr} \;=\; 0 \tag{2.15}$$

Using the velocity-force projection method developed in [13], also developed in the Appendix for this particular case, (2.15) is equivalently expressed in differential form as,

$$(dp_{t1q} - dp_{t1r})X_{qr} \;+\; (dp_{t2q} - dp_{t2B})Y_{qr} \;+\; (dp_{nq} - dp_{nr})Z_{qr} \;=\; 0 \tag{2.16}$$

Using (2.10), the tangential components in the above equations can be written as,

$$\begin{aligned} &(-\mu_q \cos\phi_q dp_{nq} + \mu_r \cos\phi_r dp_{nr})X_{qr} \\ &+(-\mu_q \sin\phi_q dp_{nA} + \mu_r \sin\phi_r dp_{nB})Y_{qr} \\ &\qquad + (dp_{nq} - dp_{nr})Z_{qr} \;=\; 0 \end{aligned} \tag{2.17}$$

Then, a relationship can be expressed between, dp_{nq} and $dpnr$, when $q \neq r$,

$$dp_{nq} = \underbrace{\left(\frac{\mu_r cos\phi_r \; X_{qr} + \mu_r sin\phi_r \; Y_{qr} + Z_{qr}}{\mu_q cos\phi_q \; X_{qr} + \mu_q sin\phi_q \; Y_{qr} + Z_{qr}}\right)}_{C_{qr}} dp_{nr} \tag{2.18}$$

Therefore, a rigid body constraint between two arbitrary points q and r in the i^{th} body can be describe using the quantity C_{qr}, such that

$$\begin{aligned} C_{qr} &= \frac{\mu_r cos\phi_r \; X_{qr} + \mu_r sin\phi_r \; Y_{qr} + Z_{qr}}{\mu_q cos\phi_q \; X_{qr} + \mu_q sin\phi_q \; Y_{qr} + Z_{qr}} \qquad \text{if} \quad q, r = 1, ..., n_i \;\; q \neq r \\ C_{qr} &= 1 \qquad \text{if} \quad q = r \end{aligned} \tag{2.19}$$

which provides a general form of the constraint between two arbitrarily configured impact points. These derived constraints are used in order to express the differential equations of motion as a function of a single, independent normal impulse parameter, dp_{nr}, without any loss of generality. Substitution of all the rigid body constraints into (2.12) yields,

$$d\boldsymbol{\vartheta} = MH\mathbf{G}dp_{nr} \tag{2.20}$$

where,

$$\mathbf{G} = \left[{\mathbf{G}_1}^T, ..., {\mathbf{G}_{N_b}}^T\right]^T \text{s.t.} \mathbf{G}_i = [C_{qr}]^T$$

Thus, with the equation in (2.20) multiple pint contacts and impacts can be analyzed with respect one independent normal impulse variable. In the following section, we shall explore the effects of stick-slip on the tangential components of the velocities and the impact forces.

2.6 Transformation to Cylindrical Coordinates

The analysis up to this point has been carried out in Cartesian coordinates, see [22, 17]. However, as mentioned before, the slip direction in the case of three-dimensional impacts can be discontinuous, therefore expressing (2.20) in cylindrical

coordinates would be more appropriate for detecting these discontinuities. A transformation is carried out to describe the velocity components in terms of cylindrical coordinates, similar to [7, 22]. The following equation shows the velocity in terms of cylindrical coordinates for points $j = 1, ..., N_p$,

$$\mathbf{v}_j = \begin{bmatrix} v_{3j-2} \\ v_{3j-1} \\ v_{3j} \end{bmatrix} = \begin{bmatrix} s_j \ \cos\phi_j \\ s_j \ \sin\phi_j \\ v_{nj} \end{bmatrix} \tag{2.21}$$

where $s_j = \sqrt{{v_{3j-2}}^2 + v_{3j-1}^2}$, $\phi_j = \tan^{-1}(v_{3j-1}/v_{3j-2})$ and v_{nj} are the normal velocities. Before implementing these relations into (2.20), a differentiation of (2.21) is needed, which gives,

$$d\mathbf{v}_j = \begin{bmatrix} \cos\phi_j & -s_j \ \sin\phi_j & 0 \\ \sin\phi_j & s_j \ \cos\phi_j & 0 \\ 0 & 0 & 1 \end{bmatrix} \begin{bmatrix} ds_j \\ d\phi_j \\ dv_{nj} \end{bmatrix} = P_j \begin{bmatrix} ds_j \\ d\phi_j \\ dv_{nj} \end{bmatrix} \tag{2.22}$$

Expressions similar to (2.22) can be obtained for all the points with corresponding terms on the right-hand side. The coefficients are collected in the form of a block diagonal matrix P,such that $P \in \mathrm{R}^{N_c X N_c}$,

$$P = \begin{bmatrix} P_1 & 0 & \cdots & \cdots & 0 \\ 0 & P_2 & \ddots & \ddots & \vdots \\ \vdots & \ddots & \ddots & \ddots & \vdots \\ \vdots & \ddots & \ddots & P_{N_p-1} & 0 \\ 0 & \cdots & \cdots & 0 & P_{N_p} \end{bmatrix}$$

Solving for the sliding velocity, sliding direction and normal velocity of each impact point using (2.20) yields,

$$d\boldsymbol{\vartheta}_{cyl} = P^{-1} M H \mathbf{G} dp_{nr} \tag{2.23}$$

The vector $d\boldsymbol{\vartheta}_{cyl}$ is the differential of $\boldsymbol{\vartheta}_{cyl}$, which is a vector containing the velocities of the points in cylindrical coordinates. P is invertible as long as the sliding velocity of all the impact point are non-zero. Otherwise, a singularity arises and matrix P is no longer invertible. Also, note that this scenario represents the point during a collision in which an impact point comes to rest at the stick-slip transition. To overcome this singularity, an event-based approach is used, similar to the contact detection scheme [23], to detect when any of the impact points reach the stick-slip transition. The numerical integration is halted and the stick-slip transition is evaluated to determine if the impact point will slip-reverse or stick. The numerical integration is then restarted using the updated slip-state of the impact point until the impact event ends or another point comes to rest. In the next section, a theory on the rigid body constraints for the impact points have been developed, such that these constraints would reduce the number of independent differential impulse variables needed to describe the velocities of the points.

2.7 Stick-Slip Transition

The development in the preceding sections are based on the condition when the contact points are in sliding phase, giving rise to tangential velocities on the impact plane. However, in a real situation there is a possibility when any given contact point can stick(halt). This feature of an impact problem is captured in the discontinuity of the coulomb's law (2.6). When a contact point sticks the magnitude of the frictional forces becomes less than $\mu_j f_{3j}$, such that it restricts the motion of the point.

As stated in [15, 16], during the impact event, when a contact point comes to rest at the stick-slip transition phase,there are two possibilities: slip-reversal or sticking. If Slip-Reversal occurs the point continues sliding in a new direction, whereas if the point sticks, the rate of change of the tangential velocities of the point becomes zero.

Thus, for a point $j = s$ where $j = 1, .., N_p$ that sticks, the tangetial velocities can be set to zero, using(2.20),

$$\begin{bmatrix} dv_{3s-2} \\ dv_{3s-1} \end{bmatrix} = \begin{bmatrix} 0 \\ 0 \end{bmatrix} = \begin{bmatrix} \mathbf{m_1} \\ \mathbf{m_2} \end{bmatrix} \begin{bmatrix} dp_{3s-2} \\ dp_{3s-1} \\ \vdots \end{bmatrix} \tag{2.24}$$

where the $\mathbf{m_1}$ and $\mathbf{m_2}$ are the row vectors of the matrix, M and comes from the following,

$$M = \begin{bmatrix} m_{1\,1} & m_{1\,2} & \cdots & m_{1\,N_c} \\ m_{2\,1} & m_{2\,2} & \cdots & m_{2\,N_c} \\ \vdots & \vdots & \ddots & \vdots \\ m_{N_c\,1} & m_{N_c\,2} & \cdots & m_{N_c\,N_c} \end{bmatrix} = \begin{bmatrix} \mathbf{m_1} \\ \mathbf{m_2} \\ \vdots \\ \mathbf{m_{12}} \end{bmatrix}$$

In addition, the Coulomb friction relation for point j is removed since the slip-state at the stick-slip transition needs to be determined. Solving for the tangential impulses yields,

$$\begin{bmatrix} dp_{3s-2} \\ dp_{3s-1} \end{bmatrix} = \begin{bmatrix} m_{3s-2\,3s-2} & m_{3s-2\,3s-1} \\ m_{3s-1\,3s-2} & m_{3s-1\,3s-1} \end{bmatrix}^{-1} \begin{bmatrix} -\mathbf{n_1} \\ -\mathbf{n_2} \end{bmatrix} \mathbf{U}\mathbf{G}dp_{nr} \tag{2.25}$$

where $\mathbf{n_1}$ and $\mathbf{n_2}$ are vectors containing elements from the M matrix,

$$\left[\begin{array}{ccc|ccc} m_{1\,1} & \cdots & m_{1\,3(s-1)} & m_{1\,3s} & \cdots & m_{1\,N_c} \\ m_{2\,1} & \cdots & m_{2\,3(s-1)} & m_{2\,3s} & \cdots & m_{2\,N_c} \\ \vdots & \vdots & \vdots & \vdots & \vdots & \vdots \\ m_{N_c\,1} & \cdots & m_{N_c\,3(s-1)} & m_{N_c\,3s} & \cdots & m_{N_c\,N_c} \end{array}\right] = \begin{bmatrix} \mathbf{n_1} \\ \mathbf{n_2} \\ \vdots \\ \mathbf{n_{12}} \end{bmatrix}$$

and $\mathbf{U}$ can be written as,

$$\mathbf{U} = [u_k]_{N_c-2} \quad \text{s.t.} \quad u_k = \begin{cases} -\mu_k \cos\phi_k & \text{if} \quad k = 3j-2 \;\; \& \;\; j \neq s \\ -\mu_k \sin\phi_k & \text{if} \quad k = 3j-1 \;\; \& \;\; j \neq s \\ 1 & \text{if} \quad k = 3j \\ 0 & \text{if} \quad 3k-2 > j > 3k \end{cases}$$

The no-slip condition is used to determine if an impact point will stick or slip-reverse.

$$\sqrt{{p_{3s-2}}^2 + {p_{3s-1}}^2} \leq \mu_k \, dp_{3s} \quad \longrightarrow \quad \frac{\sqrt{{p_{3s-2}}^2 + {p_{3s-1}}^2}}{dp_{nr}} = \bar{\mu}_s \leq \mu_s \tag{2.26}$$

where $\bar{\mu}_s$ is the critical coefficient of friction for stick for point $j = s$. For the impact point to remain in stick, $\mu_s \geq \bar{\mu}_s$ which imposes a lower bound on μ_s. If this condition is not met, then the impact point slip-reverses. It is also important to note that the calculation for this critical coefficient for stick is solely dependent on the configuration and inertia properties of the system. Whereas, during initial sliding the sliding direction ϕ_s is unpredictable due to the nonlinearities of friction, this is not the case if an impact point slip-reverses. For a point that slip-reverses, the impact point slides in a constant, unique direction [24, 15, 16, 22] and determined by,

$$\phi_s = tan^{-1}\left(\frac{m_{3s-2\,3s-2}\, m_{3s-1\,3s} - m_{3s-2\,3s-1}\, m_{3s-2\,3s}}{m_{3s-1\,3s-1}\, m_{3s-2\,3s} - m_{3s-1\,3s}\, m_{3s-2\,3s-1}}\right) \tag{2.27}$$

by way of example for point $j = s$. The sliding direction after the stick-slip transition is a function of the configuration and inertia properties of the system [24, 15, 16, 22], which is similar to the determinate of the critical coefficient of friction. Otherwise, if stick prevails, then $\bar{\mu}_s$ is used instead of μ_s in the analysis.

2.8 Energy Dissipation

The impact event consists of two phases: compression phase and restitution phase. The compression phase starts at the beginning of the impact event and ends when the normal velocity of the point becomes zero. The restitution phase starts when the normal velocity becomes positive, and ends when the body starts to separate from the ground. Figure 2.5 is taken from [1], and shows how normal work, which accounts for all the energy loss in the system, typically evolve during an impact event. In this section, the work-energy theorem is used to determine the end of the compression

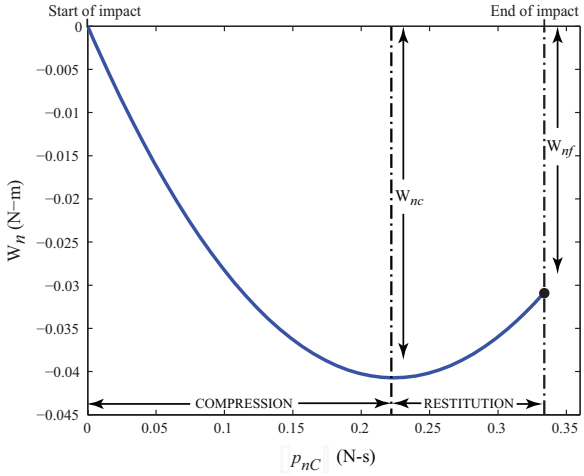

Figure 2.5. Typical Normal Work Plot during an Impact Event.

phase of the impact event, and subsequently determine the end of the restitution phase or impact event. The calculation of the work is given as the change in kinetic energy between the initial and final states of the impact as,

$$T_2 \;=\; T_1 \;+\; W_{1-2} \;=\; T_1 \;+\; U_1 \;-\; U_2 \;+\; (W_{1-2})_d \tag{2.28}$$

where T_i and U_i are the kinetic and potential energy at state i, and $(W_{1-2})_d$ is the non-conservative, or dissipative, work done on the system between states 1 and 2. In this work, the potential energy terms U_1 and U_2 are neglected due to the hard impact assumptions, or negligible deformation, from the strict adherence to rigid body modeling.

$$W_{1-2} \;=\; T_2 - T_1 \;=\; \frac{1}{2}\,\dot{\mathbf{q}}^T(t+\epsilon)M\;\dot{\mathbf{q}}(t+\epsilon) - \frac{1}{2}\,\dot{\mathbf{q}}^T(t)M\;\dot{\mathbf{q}}(t) \tag{2.29}$$

Consider the normal work done during a collision to be the integration of the dot product between the normal force and displacement as,

$$\begin{aligned} W_n &= \int \mathbf{F}^T d\mathbf{x} = \sum_{i=1}^{N_c} \int f_i dx_i \\ &= \sum_{i=1}^{N_c} \int dp_i \frac{dx_i}{dt} = \int \vartheta^T d\mathbf{p} = \int \vartheta^T \mathbf{G} dp_{nr} \end{aligned} \tag{2.30}$$

where the rigid body constraints are implemented and the normal work is determined as a function of a single, independent normal impulse parameter. And written in differential form,

$$\frac{dW_n}{dp_{nr}} = \vartheta^T \mathbf{G} \tag{2.31}$$

Notice that (2.31) is differentiated with respect to dp_{nr}. By equating (2.31) to zero yields the normal impulse p_{nc} at the end of the compression phase for the system, which is a function of the normal velocities of the impact points and the constraint equations derived. Also, p_{nc} and subsequently W_{nc} may change if the end of the impact event is not reached if an impact point comes to rest at the stick-slip transition. In the event that multiple shifts occur in the normal work plot, then the normal work curve for the latter shift is used with the ECOR to determine the net normal work W_{nf} for the impact event.

The set of first order, nonlinear ODE's in (2.20), the rigid body constraints as in (2.18), and the normal work in (2.31) are formulated into a state function $\mathbf{y}$ as,

$$\begin{aligned} \frac{d\mathbf{y}}{dp_{n\mathrm{r}}} &= f(p_{n\mathrm{r}}, \{\vartheta, W_n\}) \\ \text{IC: } \mathbf{y}(\mathbf{0}) & \end{aligned} \tag{2.32}$$

where $\mathbf{y}(0)$ is a vector of the initial conditions for the variables that appear in (2.32).

Stronge's energetic coefficient of restitution (ECOR) is applied to determine the net normal work for an impact event as,

$$W_{nf} = (1 - e_*^2) W_{nc} \tag{2.33}$$

where $e_* \in [-1, 1]$ is a *global* ECOR which accounts for the energy dissipated by the system in an impact event. In this work, $e_* < 0$ means that in a simultaneous, multiple point collision subsequent impact events may begin while an initial impact event has not completed its compression phase. The value of e_* is usually not known

in a predictive sense, unless a good understanding of the material properties and physical behavior of the system is accounted for, as in [25, 26], which is not the goal in this work. Alternately, e_* functions more as a parameter to estimate the energy dissipated and its value in the present framework can be selected to correlate with experimental studies of an equivalent system.

CHAPTER 3

SIMULATION RESULTS: BLOCK

The method described in the previous chapter can be used for analyzing surface impacts by considering any number of points. This chapter would present some simulation results on impacting block using the same method. The simulation results provided in this chapter were generated for two different cases: 1) Block undergoing central/collinear impact with the ground and 2) Block undergoing non-collinear impact with the ground(rocking block). Two simulation results are provided for either of the cases. One of them is based on four point analysis and the other one is based on eight point analysis. These results are then compared to show that the post-impact behavior of an impacting body is independent of the number of points are considered for analysis.

3.1 Central/Collinear Impact

This section presents the simulation results for the first case i.e collinear impact. In order to simulate a collinear impact, the block is dropped from some height in a flat configuration, such that when the block collides with the ground the direction of the impact is normal to the impact plane. Figure 3.1(a) and 3.1(b) shows the initial conditions of the four point block and the eight point block respectively. Figure 3.2(a) and 3.2(b) shows the motion captured images of the blocks before and after impact. It can be observed that both blocks rebound back in a flat configuration. A clearer representation of the pre/post impact behavior is presented in figures 3.3 and 3.4, which shows the position plots of the contact points w.r.t time.

Note that plots in 3.3(a), 3.3(b), 3.3(c) and 3.3(d) are identical to the plots in 3.4(a), 3.4(b), 3.4(c) and 3.4(h) respectively. These plots correspond to the same contact points (the points at the vertices) that are considered in both cases. This shows that the post-impact behavior of the block doesn't change based on the number of points selected for analysis. Figure 3.5, shows a comparison between the velocities in four point and eight point impact analysis. In these plots the normal velocities are drawn in magenta, whereas the sliding direction is drawn in green. Figure 3.5(a) which is showing a four point impact consists of four normal velocity, four sliding direction and four sliding velocity plots. Similarly, figure 3.5(b) which is showing an eight point impact, consists of eight normal velocity, eight sliding direction and eight sliding velocity plots. However, in either of these plots only one normal velocity and one sliding direction can be observed. This is because all the normal velocity, sliding direction and sliding velocity plots are overlayed on one another. Since, the blocks are undergoing a central/collinear impact and rebounding back with a flat configuration, all the normal velocities at the contact point increase at the same rate during impact. The initial sliding direction and sliding velocity is zero, as a result the block remains sticking through out the impact. Note, that in either case the velocities at the end of the impact is exactly same, which further proves the fact that the post-impact behavior of the impacting body doesn't depend on the number of points chosen for impact analysis. Figure 3.6 compares the normal work during the impact event for either cases. It can be observed that the normal work at the end of impact is same for both the cases, which means that energy loss due to the impact is equal for both the cases.

3.2 Non-Collinear Impact

In this section, simulation results for non-collinear impact would be discussed. Similar to the analysis in the previous section, a block is dropped from some height so that it undergoes impact. However, unlike the previous case, in this analysis the block is dropped at an angle such that it lands on one of the edges. In this case, block would undergo a series of impacts before it settles to a stable contact. Figure 3.7 shows the initial conditions for both the blocks. As the the blocks go through the series of impacts, the motion capture image as in figure 3.8 shows the block switching contacts, as it settles down. Figures 3.9 and 3.10 show the position plots of the impact points. Upon comparison, the plots for the same impact points in the either cases (3.9(a) - 3.10(a), 3.9(b) - 3.10(b), 3.9(c) - 3.10(c), and 3.9(d) - 3.10(h)), appear to have identical behavior in both four-point and eight-point analysis cases, as it was observed in the case of collinear impact. Figure 3.11 shows the velocity plots for the series of six consecutive four point and eight point impacts that take place between the block and the ground. Again on these plots, these plots the normal velocities are represented in magenta, sliding velocities in blue, and the sliding directions in green. Figures 3.11(a) and 3.11(b) are the velocity plots during the first impact, which are identical to each other. The first impact occurs at one edge of the block, as a result of which, we can notice the normal velocities corresponding to the contact points situated on that particular edge increasing till a positive value, while the other points continue to have the same normal velocity through the impact. Also, note that the impact points experience a change in the sliding velocities. The initial conditions set at the end of the first impact, makes the block rebound, such that the other points experiences impact. 3.11(c) and 3.11(d) shows the velocity plots for the second impact. In this case, for the eight point impact the velocities of the additional points are not identical to the other four, as a result separate plots can

be seen for these velocities. Again a very similar trend can be observed in this case, where the normal velocities of some points(the ones that are experiencing impact) are going from a negative to a positive value, while the normal velocities for remaining points remain unchanged. Figures 3.11(e), 3.12(a), 3.12(c), and 3.12(e) show the subsequent impacts for the four point case, while the figures 3.11(f), 3.12(b), 3.12(d) and 3.12(f) show the subsequent impacts for eight point analysis case. All these plots, show a trend that is very similar to the one observed in the first two. One of the key observation over here is that the post-impact velocities for specific points are the same in both four point as well as eight point analysis. The normal work plots for all these different impacts are shown in figures 3.13 and 3.14. Once again, similar amount of energy loss can be observed for both cases, which proves that the energy loss in the system doesn't depend on the number of points selected for analysis.

Thus, from all the results presented in this chapter it is very evident that the velocities and energy loss during the impact event and the post-impact behavior after an impact doesn't depend upon the number of points selected for analysis. This is a very crucial result, as this gives us the liberty to analyze large number of points during impact, and consequently alleviating the need for analysis on how to select these points. If a large number of points are used for analysis, they could be evenly spread through out the surface of the impact, similar to a grid or a mesh, such that impact analysis may cover all possible scenarios.

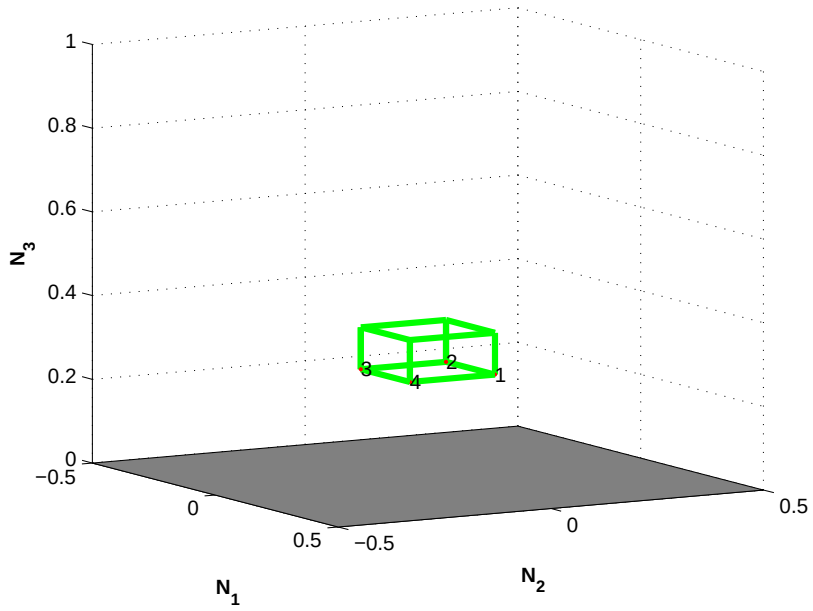

(a) Block with four point analysis

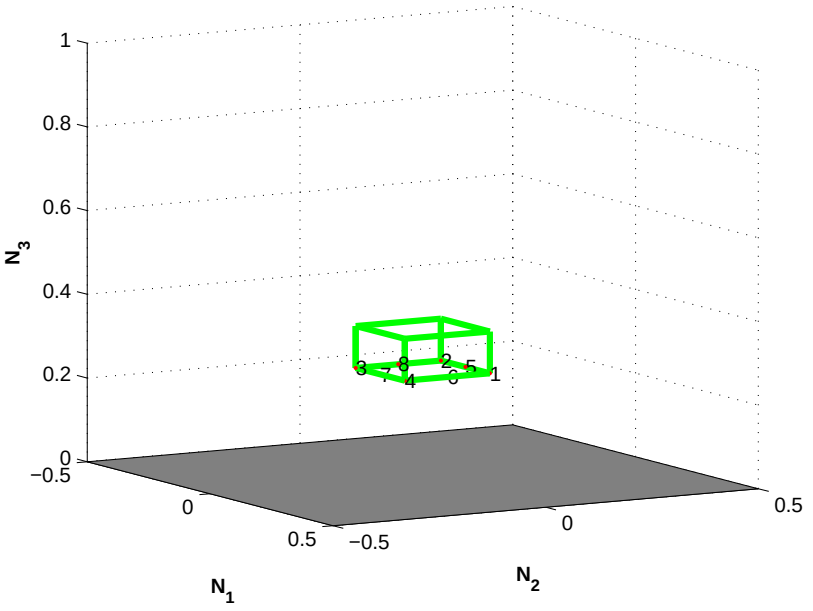

(b) Block with eight point analysis

Figure 3.1. Blocks with Four and Eight Points Central Impact.

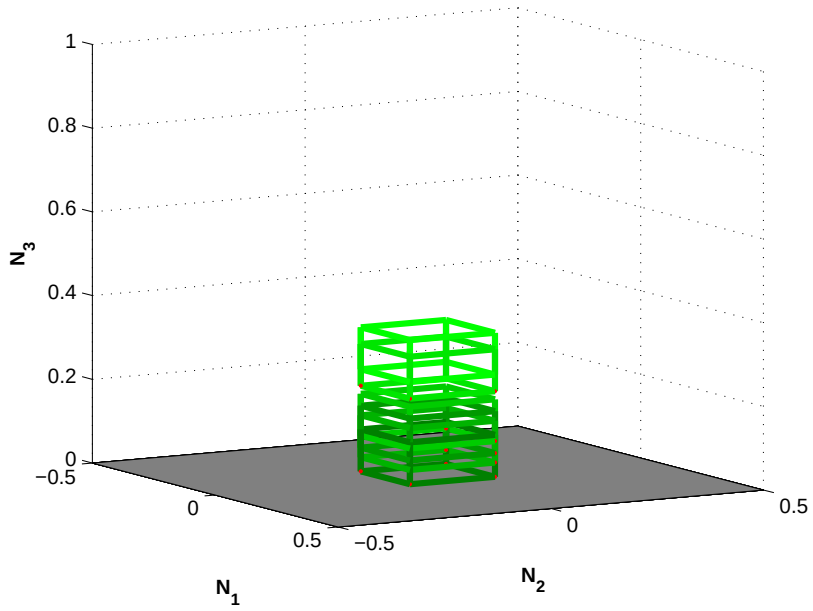

(a) Block motion capture four point impact

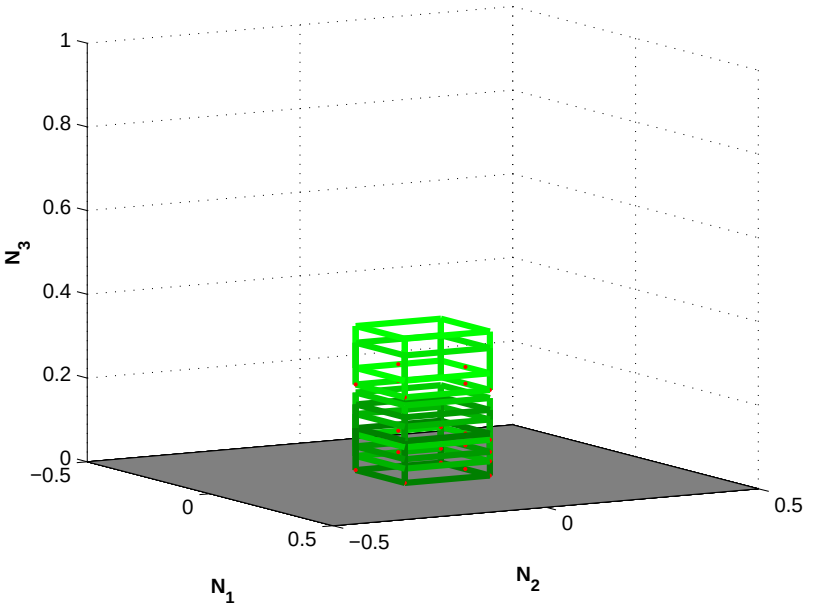

(b) Block motion capture eight point impact

Figure 3.2. Motion Capture of the Block undergoing Central Impact.

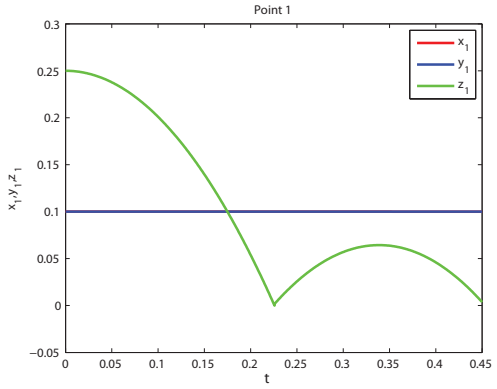

(a) Position of Point 1

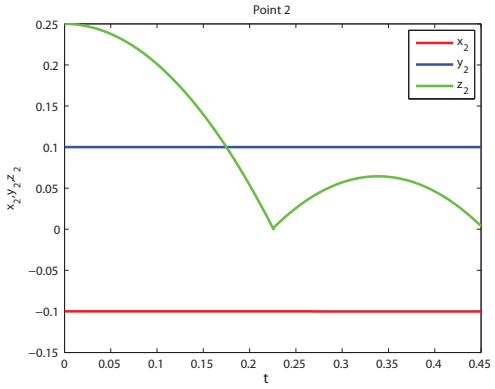

(b) Position of Point 2

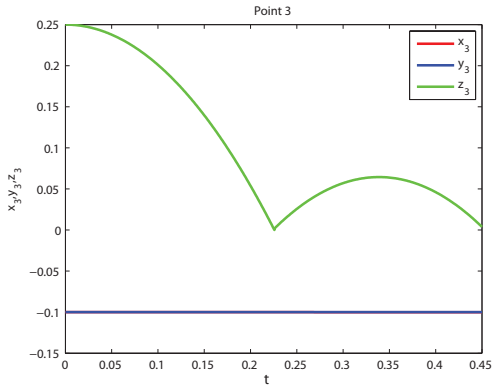

(c) Point of Point 3

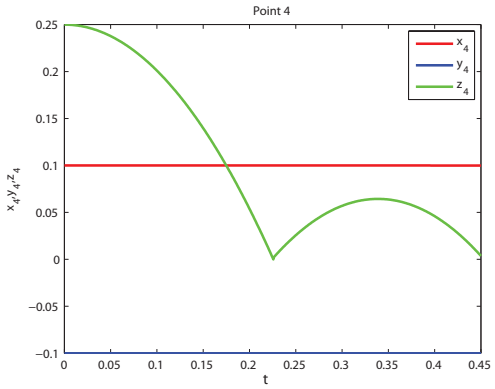

(d) Point of Point 4

Figure 3.3. Four-Point Position Plot for Block undergoing Central Impact.

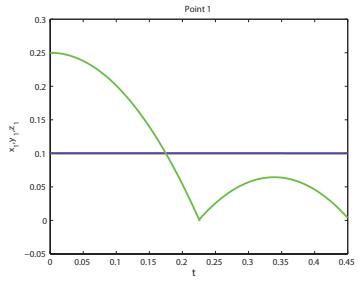

(a) Position of Point 1

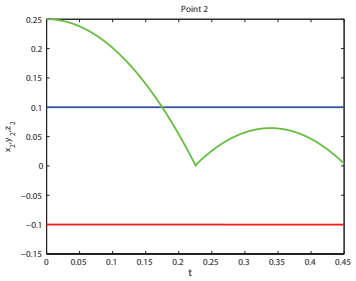

(b) Position of Point 2

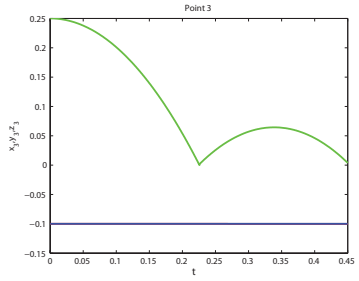

(c) Position of Point 3

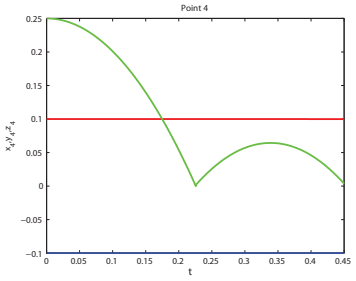

(d) Position of Point 4

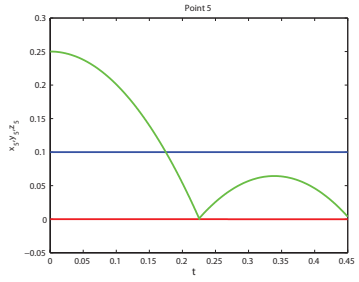

(e) Position of Point 5

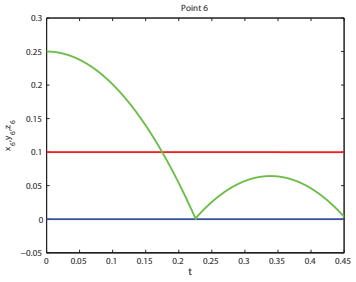

(f) Position of Point 6

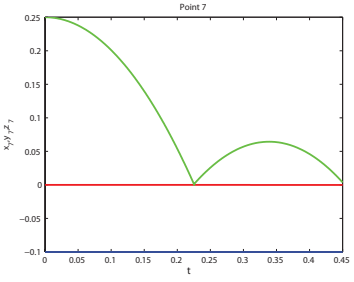

(g) Position of Point 7

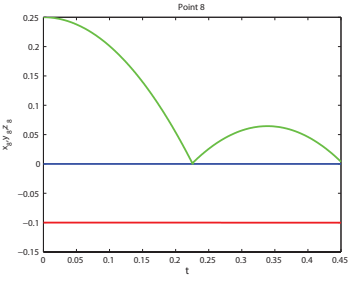

(h) Postion of Point8

Figure 3.4. Eight-Point Position Plot for Block undergoing Central Impact.

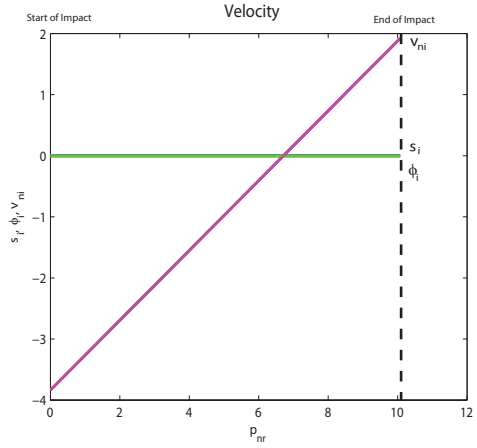

(a) Four Point Impact Velocity Plots

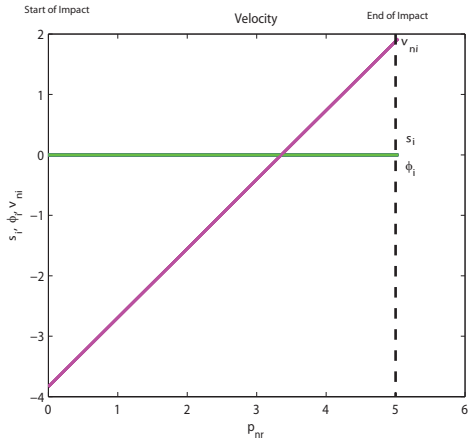

(b) Eigth Point Impact Velocity Plots

Figure 3.5. Velocity Plot Comparison for Central Impact.

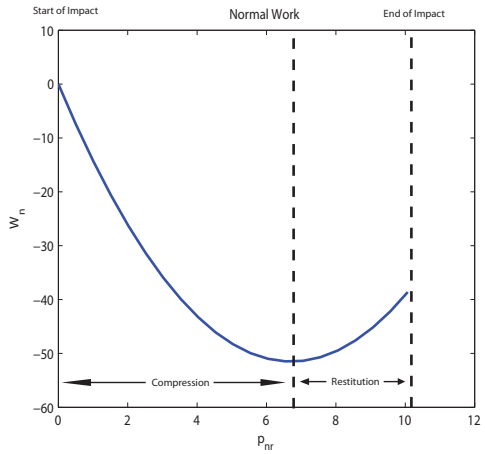

(a) Four Point Impact Normal Plots

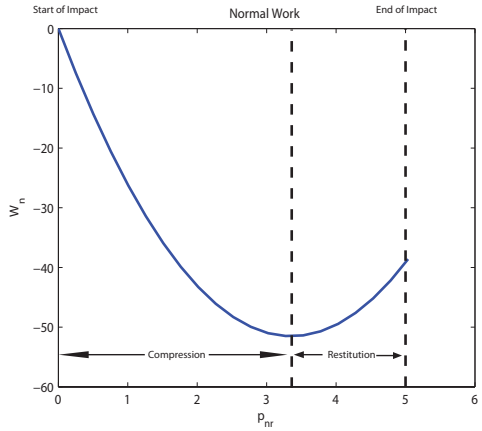

(b) Eight Point Impact Normal Work Plots

Figure 3.6. Work Plot Comparison for Central Impact.

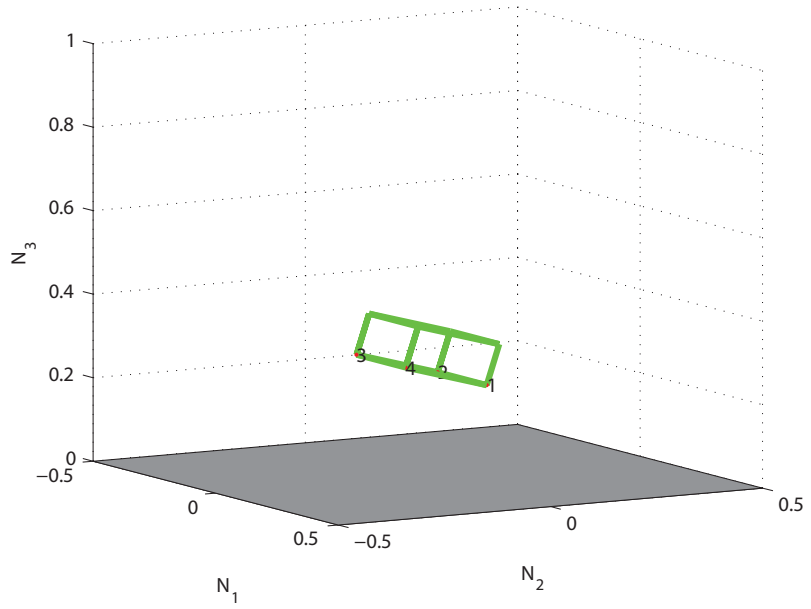

(a) Block with four point analysis

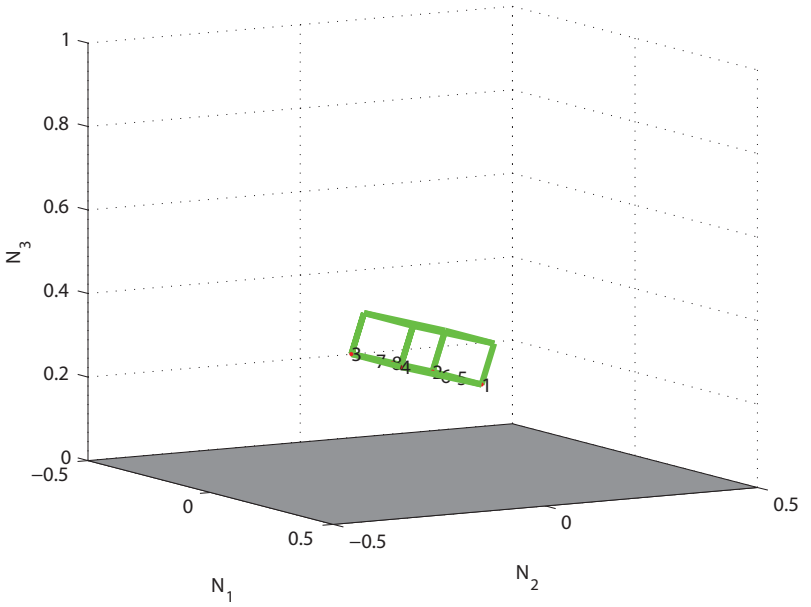

(b) Block with eight point analysis

Figure 3.7. Blocks undergoing Four and Eight-Point Non-collinear Impact.

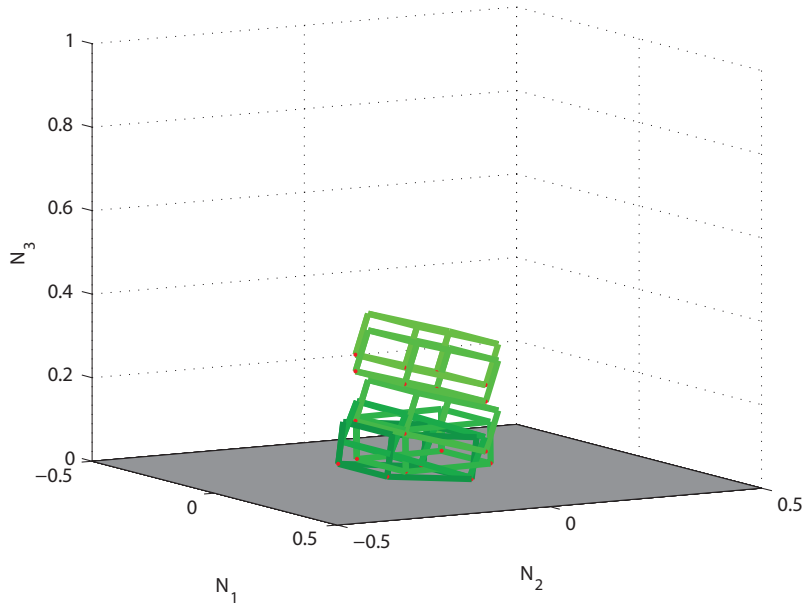

(a) Block motion capture for Four-Point Impact

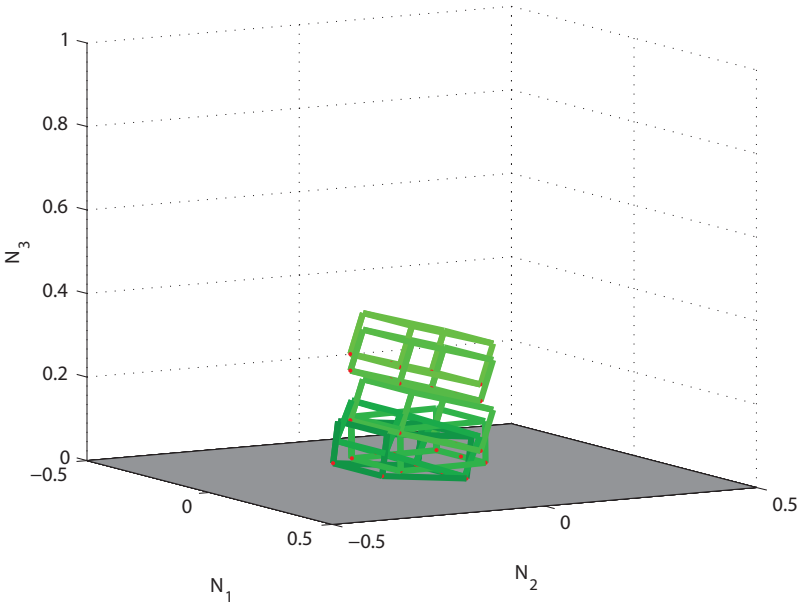

(b) Block motion capture for Eight-Point Impact

Figure 3.8. Motion Capture of the Block undergoing Non-collinear Impact.

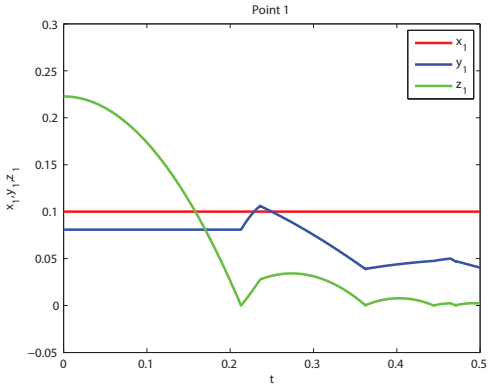

(a) Position Plot for Point 1

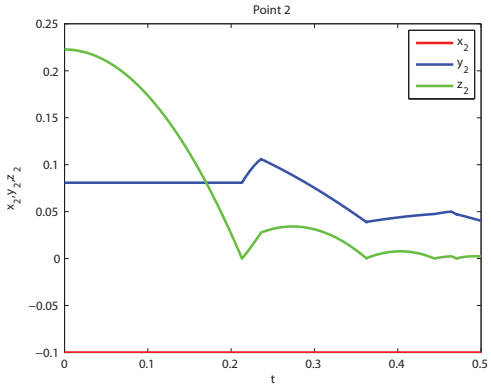

(b) Position Plot for Point 2

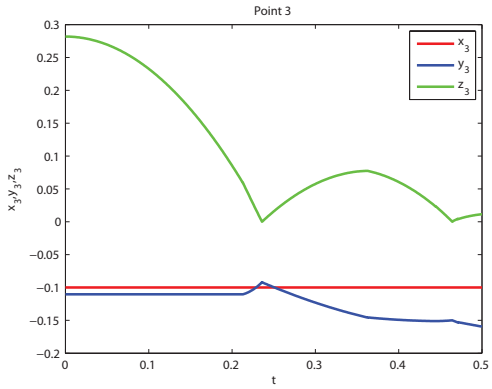

(c) Position Plot for Point 3

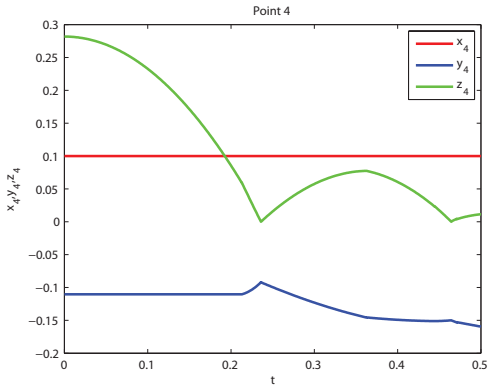

(d) Position Plot for Point 4

Figure 3.9. Four-Point Position Plot for Block undergoing Non-Collinear Impact.

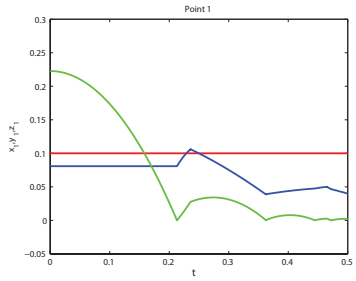

(a) Position Plot for Point 1

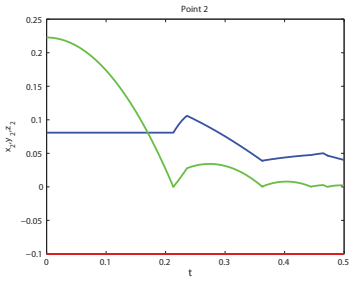

(b) Position Plot for Point 2

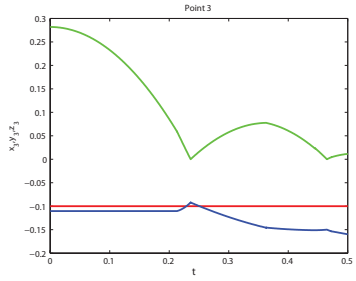

(c) Position Plot for Point 3

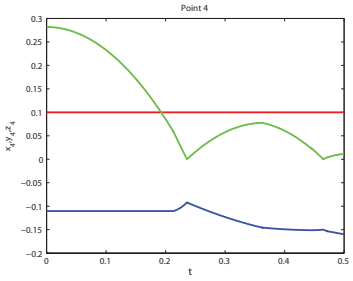

(d) Position Plot for Point 4

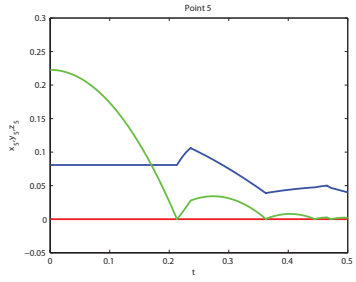

(e) Position Plot for Point 5

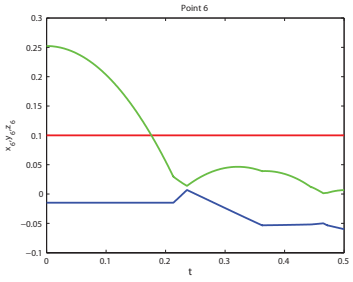

(f) Position Plot for Point 6

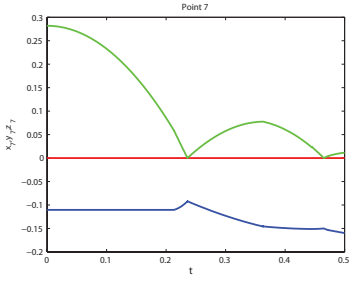

(g) Position Plot for Point7

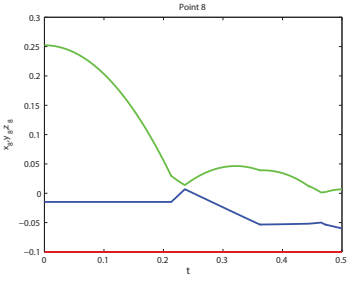

(h) Position Plot for Point8

Figure 3.10. Eight-Point Position Plot for Block undergoing Non-Collinear Impact.

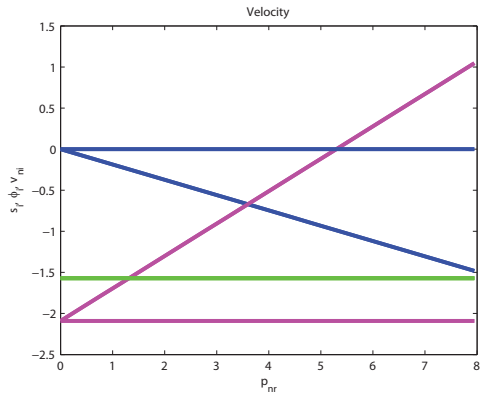

(a) First Four-Point Impact Velocity Plot

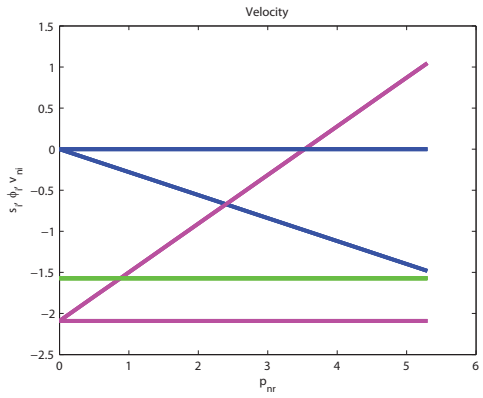

(b) First Eight-Point Impact Velocity Plot

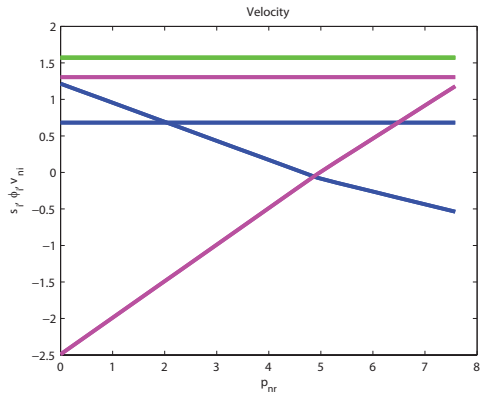

(c) Second Four-Point Impact Velocity Plot

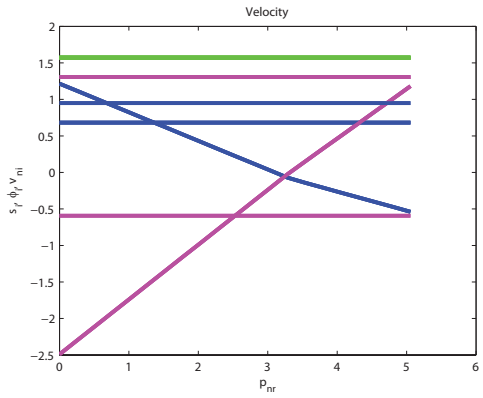

(d) Second Eight-Point Impact Velocity Plot

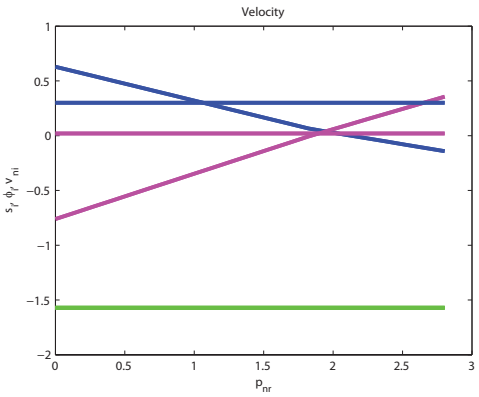

(e) Third Four-Point Impact Velocity Plot

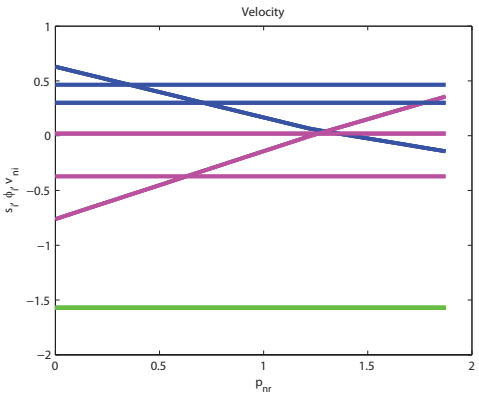

(f) Third Eight-Point Impact Velocity Plot

Figure 3.11. First Three Impacts Velocity Plots for Block undergoing Non-Collinear Impact.

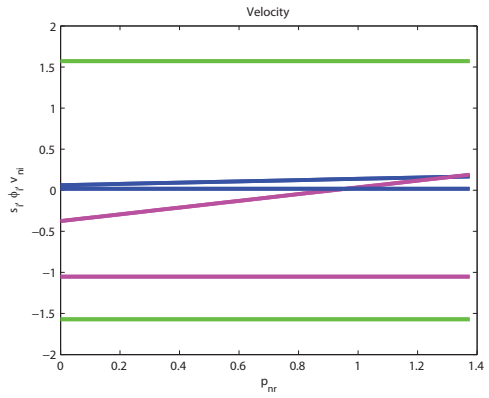

(a) Fourth Four-Point Impact Velocity Plot

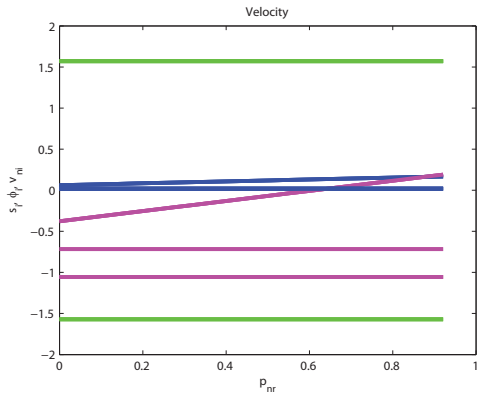

(b) Fourth Eight-Point Impact Velocity Plot

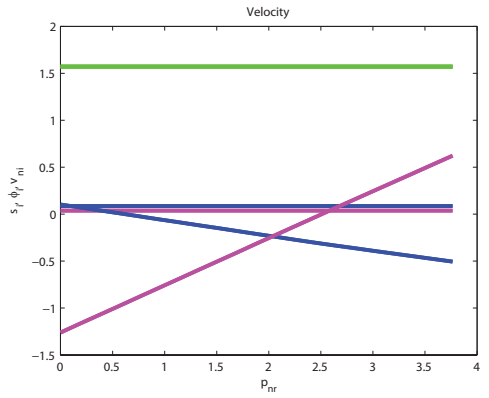

(c) Fifth Four-Point Impact Velocity Plot

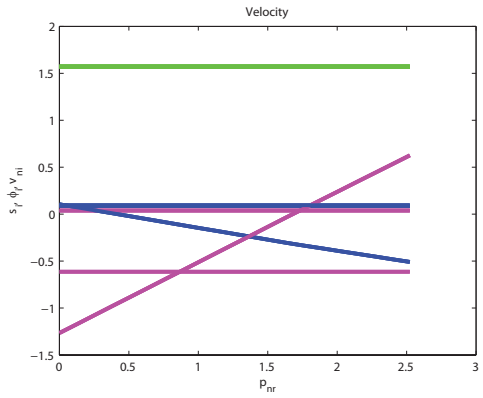

(d) Fifth Eight-Point Impact Velocity Plot

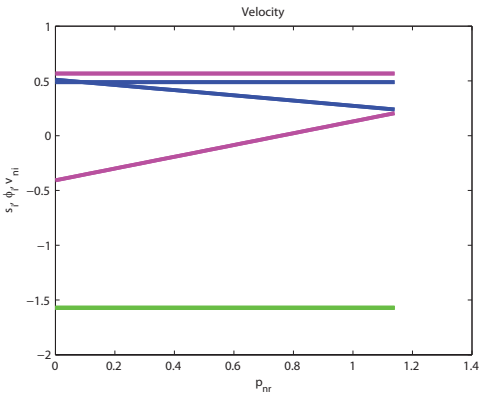

(e) Sixth Four-Point Impact Velocity Plot

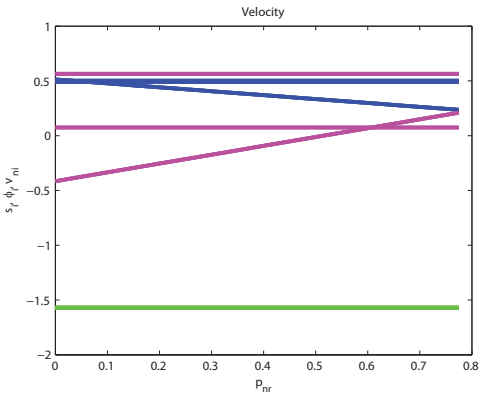

(f) Sixth Eight-Point Impact Velocity Plot

Figure 3.12. Last Three Impacts Velocity Plots for Block undergoing Non-Collinear Impact.

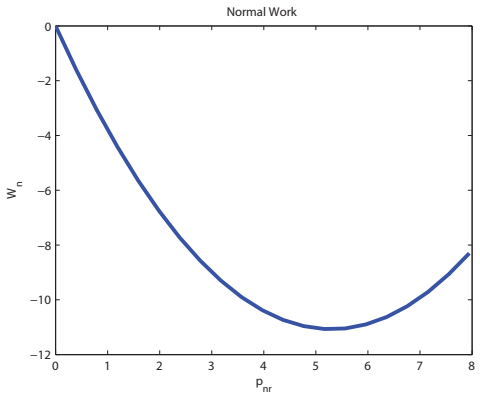

(a) First Four-Point Impact Normal Work

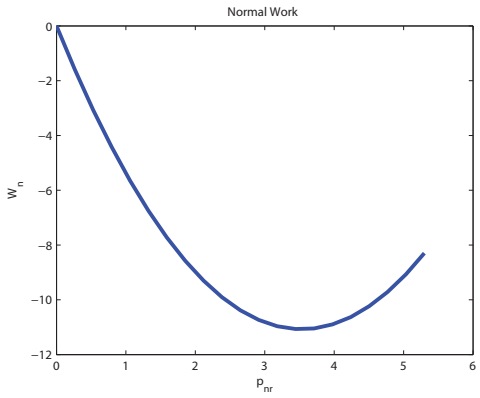

(b) First Eight-Point Impact Normal Work

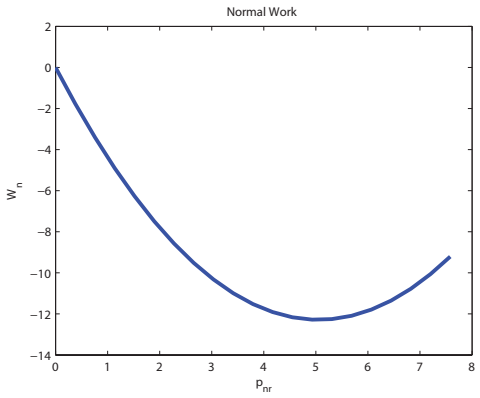

(c) Second Four-Point Impact Normal Work

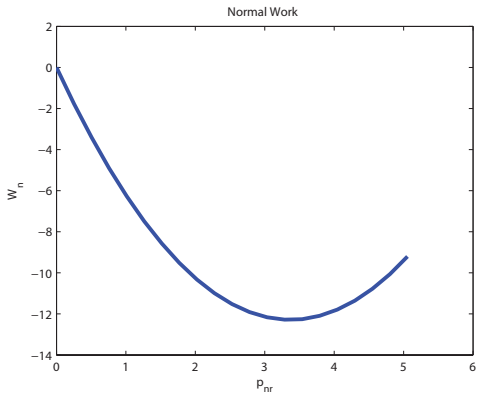

(d) Second Eight-Point Impact Normal Work

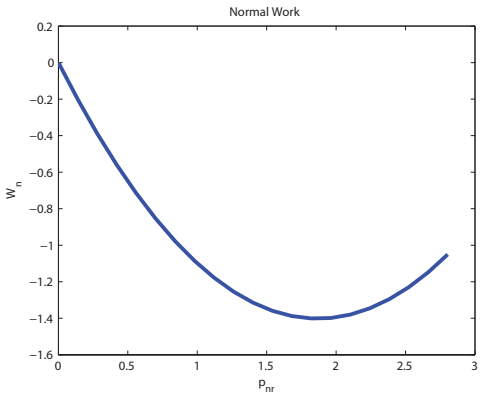

(e) Third Four-Point Impact Normal Work

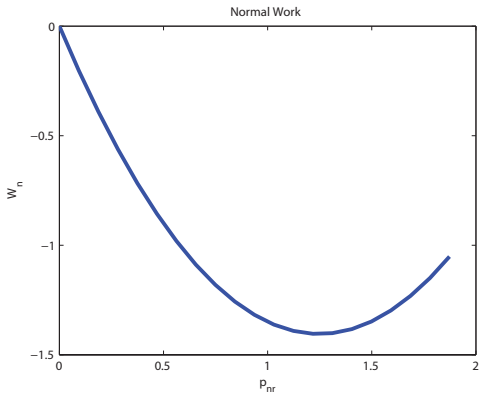

(f) Third Eight-Point Impact Normal Work

Figure 3.13. First Three Impacts Normal Work Plots for Block undergoing Non-Collinear Impact.

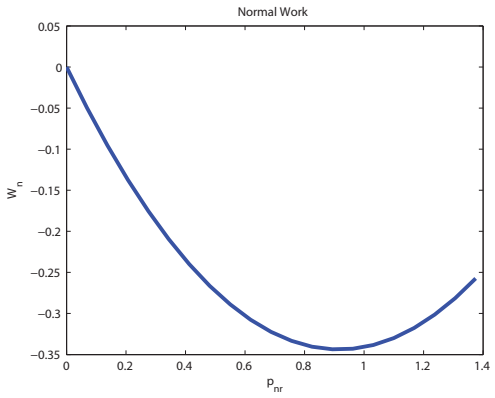

(a) Fourth Four-Point Impact Normal Work

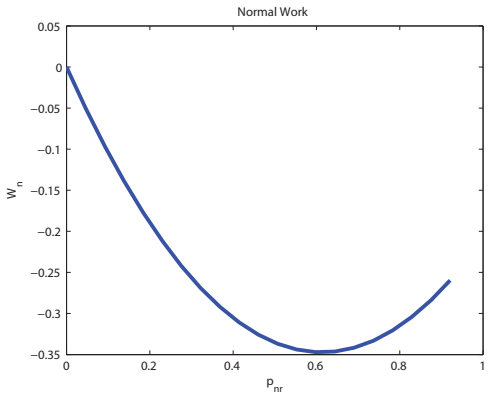

(b) Fourth Eight-Point Impact Normal Work

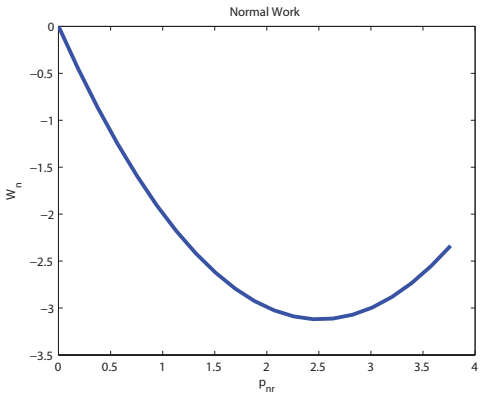

(c) Fifth Four-Point Impact Normal Work

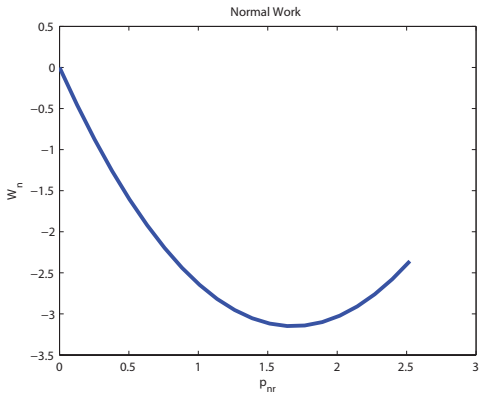

(d) Fifth Eight-Point Impact Normal Work

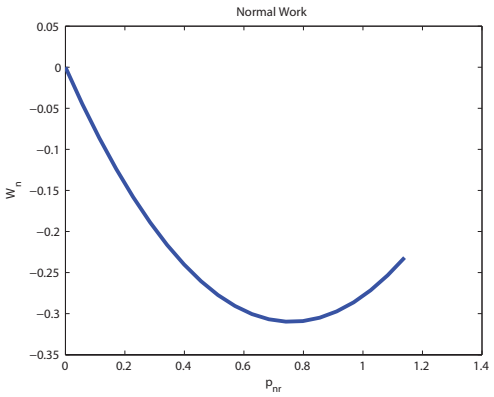

(e) Sixth Four-Point Impact Normal Work

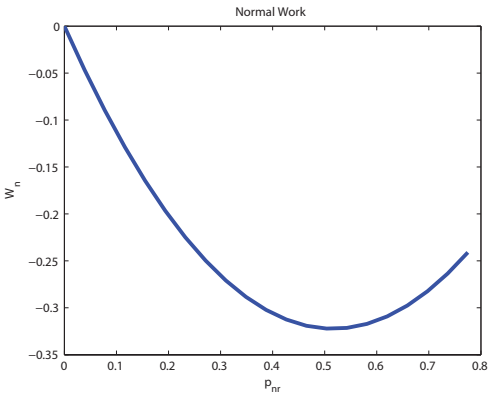

(f) Sixth Eight-Point Impact Normal Work

Figure 3.14. Last Three Impacts Normal Work Plots for Block undergoing Non-Collinear Impact.

CHAPTER 4

ROBOT CONTROL

4.1 Controller Design

The goal of this chapter is to detail the control techniques implemented in this work to achieve walking locomotion in a bipedal system. Most of the techniques discussed in this chapter are based on [27],[28],[29],[30],[31]. A position and velocity based control strategy has been implemented on this work to achieve the desired walking motion by the robot.

All robotic manipulation using position based control is essentially a trajectory tracking problem for a controller. As a result, a reference signal needs to be fed into the control system. In this case, the reference signals were generated using geometric body point trajectory generation. A desired state is estimated using the reference signal and compared with the actual state of the system, to generate an error signal that is used to drive the system. The system is assumed to be fully observable and free of noise in this work. Therefore, in the simulation environment the full state of the system was used for control and no stochastic noise were added to the system.

4.2 Trajectory Generation

Trajectories in the configurational space as a function of time are used for the purpose of providing guidance(or reference signals) to the controller. For complex mechanisms like bipedal robots, it is not easy to find configurational space trajectories for the walking motion directly without performing an inverse map from operational space of the robot. The approach used in this work deals with generating desired

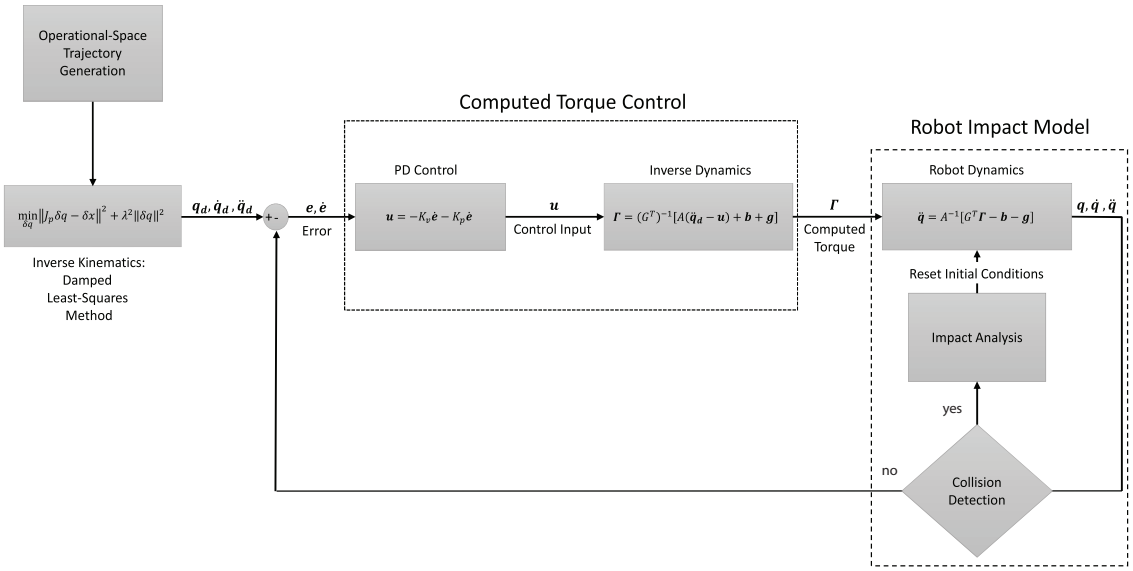

Figure 4.1. Feedback Control System Schematic.

geometric trajectories in the operational space of the robot and converting them back in terms of the configurational space for guidance.

The algorithm used for the trajectory generation can be best represented with the help of a flowchart, as provided in figure(4.2). Three body points of the robot are sufficient to generate the trajectories necessary for the walking task. The three body points that are used in this case are the position of the center of mass and the bases of the two feet of the robot. The trajectory generation as shown in figure(4.2), considers the position of each desired ground contact point or walking step as a waypoint in the overall trajectory. At the beginning of the simulation two waypoints in terms of the horizontal direction are initialized for each foot, xl_{wpi}, xl_{wpf}, xr_{wpi} and xr_{wpf}. These waypoints are the horizontal components of the initial and final positions for the first step. In case of the foot that remains grounded the initial and final waypoints are set

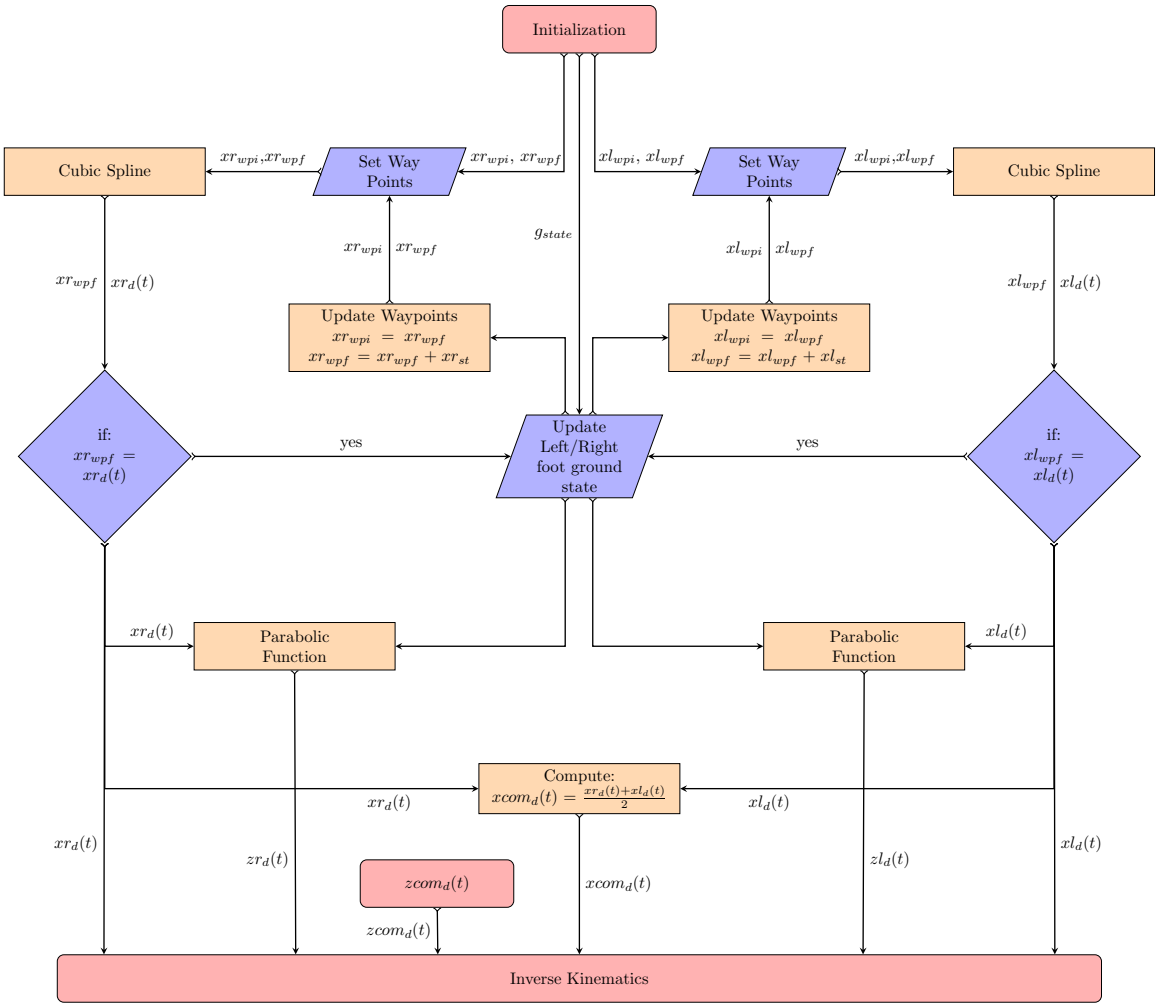

Figure 4.2. Geometric Trajectory Generation in Operational Space.

equal. Another parameter, g_{state} is initialized keeps track of the foot that is grounded; this parameter switches its state after every step and used to update the waypoints as the robot transitions from one step to another.

A cubic spline function with respect to time t, is used between waypoints to compute desired horizontal position components $xl_d(t)$ and $xr_d(t)$ for the left and right feet respectively [31],

$$xl_d(t) = xl_{wpi}\left[2(t-t_i)^3 - 3(t-t_i)^2 + 1\right] + xl_{wpf}\left[-2(t-t_i)^3 + 3(t-t_i)^2\right]$$

$$xr_d(t) = xr_{wpi}\left[2(t-t_i)^3 - 3(t-t_i)^2 + 1\right] + xr_{wpf}\left[-2(t-t_i)^3 + 3(t-t_i)^2\right] \quad (4.1)$$

The quantity t_i in the above equations is the time at the start of every waypoint. t_i is reset every time a waypoint is updated. The parameter g_{state} keeps track of the event when the right/left foot reaches a waypoint and updates the waypoints and t_i.

$$\textbf{if}: \quad xl_d(t) = xl_{wpf} \qquad \textbf{then}: \quad g_{state} = 1$$

$$\textbf{if}: \quad xr_d(t) = xr_{wpf} \qquad \textbf{then}: \quad g_{state} = 2 \quad (4.2)$$

Using this framework, whenever g_{state} changes value, t_i is reset to the current value of time. Similarly, the waypoints are updated using g_{state},

$$\textbf{if}: \quad g_{state} = 1 \qquad \textbf{then}: \begin{cases} xl_{wpi} = xl_{wpf} \\ xr_{wpi} = xr_{wpf} \\ xr_{wpf} = xr_{wpf} + xr_{st} \end{cases}$$

$$\textbf{if}: \quad g_{state} = 2 \qquad \textbf{then}: \begin{cases} xl_{wpi} = xl_{wpf} \\ xl_{wpf} = xl_{wpf} + xl_{st} \\ xr_{wpf} = xr_{wpf} \end{cases} \quad (4.3)$$

Where xl_{st} and xr_{st} are the stride lengths of the robot in left and right feet, respectively. Now, the equations in (4.1) can also be used to determine the desired horizontal position component of the center of mass of the robot,

$$xcom_d(t) = \frac{xl_d(t) + xr_d(t)}{2} \quad (4.4)$$

In order to find the desired vertical position components(when in flight) of the legs a parabolic function can be used, and when a foot is grounded the vertical position component is set to zero,

$$\textbf{if}: \quad g_{state} = 1 \quad \textbf{then}: \quad \begin{cases} zl_d(t) = 0 \\ zr_d(t) = z_{max} - \frac{z_{max}}{\left(\frac{xr_{wpf} - xr_{wpi}}{2}\right)^2}\left[xr_d(t) - xr_{wpi} - \frac{xr_{wpf} - xr_{wpi}}{2}\right]^2 \end{cases}$$

$$\textbf{if}: \quad g_{state} = 2 \quad \textbf{then}: \quad \begin{cases} zl_d(t) = z_{max} - \frac{z_{max}}{\left(\frac{xl_{wpf} - xl_{wpi}}{2}\right)^2}\left[xl_d(t) - xl_{wpi} - \frac{xl_{wpf} - xl_{wpi}}{2}\right]^2 \\ zr_d(t) = 0 \end{cases} \tag{4.5}$$

In this work, the walking locomotion is restricted to be along a straight path, without any change in direction. However, the method described above could be easily extended for another horizontal component of the position vector with equations similar to (4.1-4.4), and the vertical component can calculated with an equation similar to (4.3) An advantage of having positions of the control body points as a function of time is that the relevant equations between the numbers (4.1-4.3) can be differentiated w.r.t time to for the velocities and accelerations. However, in the interest of space, these equations are not shown in this thesis. Once the desired control point trajectories for position, velocity and acceleration are obtained, an inverse kinematic analysis is required for generating the desired joint(configurational) space coordinates, velocities and accelerations.

4.3 Configurational Space Computed Torque Control

In this section, the method used for performing the inverse kinematic analysis is discussed. Then a discussion is provided about the control technique implemented on the robot simulation, to generate a walking trajectory. The inverse kinematic analysis is performed using an iterative damped leastsquare method(also known as

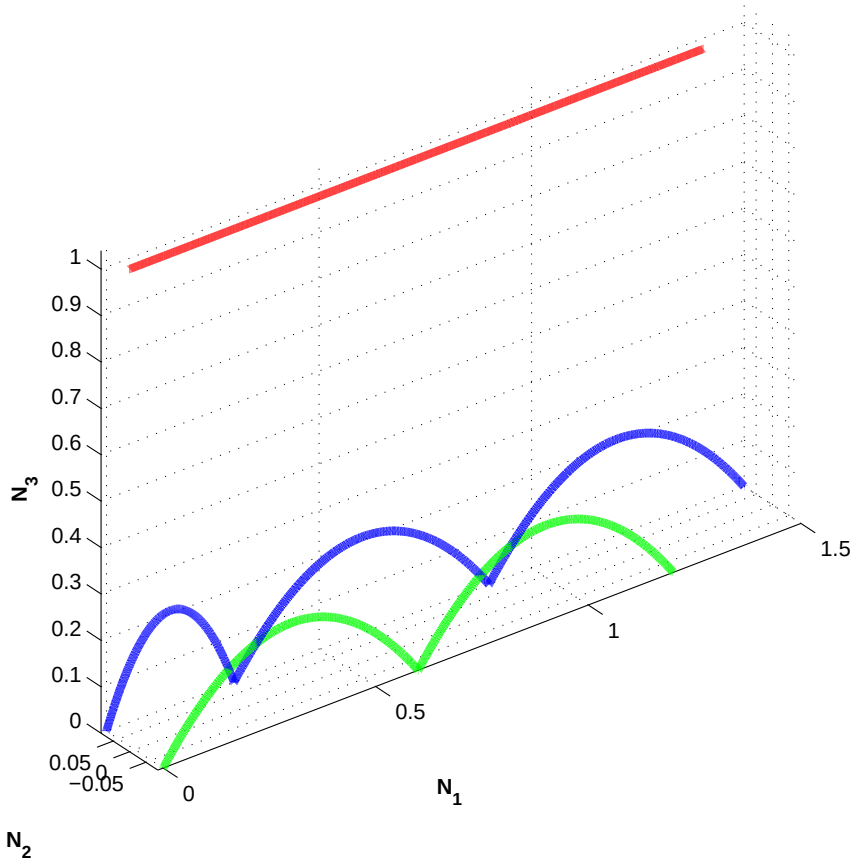

Figure 4.3. Desired Trajectory.

the Levenberg-Marquard Method) [28],[27],[29]. Recursive methods usually make use of the jacobian matrix to estimate a change in the joint space variables, such that this change corresponds to a desired change in operational space variable,

$$\nabla \mathbf{x} = J_p \nabla \mathbf{q} \tag{4.6}$$

where, $\nabla \mathbf{x}$ is the desired change in the operational space variables. $\nabla \mathbf{x}$ in this case would be the difference between actual position of a control body point and the would be the difference between actual position of a control body point and the desired position, as computed through the methods described in the section (4.2). J_p is a block of the jacobian matrix containing the jacobian row vectors of the body

points corresponding to the ones being controlled. $\nabla\mathbf{q}$ is the change in joint space coordinates that needs to be optimized such that, $\nabla\mathbf{x} \rightarrow 0$. In the damped least square method, (4.6), is reformulated as the following optimization problem,

$$\min_{\nabla\mathbf{q}} \|J_p\nabla\mathbf{q} - \nabla\mathbf{q}\|^2 + \lambda^2\|\nabla\mathbf{q}\|^2 \tag{4.7}$$

where λ is a damping coefficient.

Thus, for a given tolerance *tol*, initial set of generalized coordinates $\mathbf{q_{in}}$, initial body point positions $\mathbf{x_{in}}$ and a desired body point positions $\mathbf{x_d}$, a set of generalized coordinates can be computed that correspond to the set of desired body point positions, using the Levenberg-Marquard method, as stated in (4.7). The first step in this computation is to set the initial set of generalized coordinates equal to the desired generalized coordinate.

$$\mathbf{q_d} = \mathbf{q_{in}} \tag{4.8}$$

This process can be performed recursively by first computing an operational space error correction vector,

$$\nabla\mathbf{x} = \mathbf{x_d} - \mathbf{x_{in}} \tag{4.9}$$

Then using this error correction vector to compute the corresponding change in generalized coordinates,

$$\nabla\mathbf{q} = {J_p}^T\left({J_p}^T J_p + \lambda I\right)^{-1}\nabla\mathbf{x} \tag{4.10}$$

Note, that ${J_p}^T\left({J_p}^T J_p + \lambda I\right)^{-1}$ may not be a square matrix, and so a generalized inverse needs to be performed. A variety of methods exist for performing generalized inverse on over- and under-constrained system of equations, any of which could be chosen as appropriate for the specific problem. The change in generalized coordinates $\nabla\mathbf{q}$ is then used to update the desired generalized coordinates,

$$\mathbf{q_d} = \mathbf{q_d} + \nabla\mathbf{q} \tag{4.11}$$

These steps are repeated until,

$$\|\nabla \mathbf{q}\| \leq tol \tag{4.12}$$

The body point jacobian matrix J_p can again be used for computation of the desired configurational space velocities. The desired operational space velocities generated by taking the time-derivative of the equations (4.1-4.4), can be related to the desired configurational space velocities using the following equation,

$$\dot{\mathbf{x}}_\mathbf{d} = J_p \dot{\mathbf{q}}_\mathbf{d} \tag{4.13}$$

Taking the time derivative of the above equation gives,

$$\ddot{\mathbf{x}}_\mathbf{d} = \dot{J}_p \dot{\mathbf{q}}_\mathbf{d} + J_p \ddot{\mathbf{q}}_\mathbf{d} \tag{4.14}$$

Therefore, the configurational space velocities and accelerations can be obtained with the help of a pseudoinverse,

$$\dot{\mathbf{q}}_\mathbf{d} = {J_p}^\dagger \dot{\mathbf{x}} \tag{4.15}$$

and,

$$\ddot{\mathbf{q}}_\mathbf{d} = {J_p}^\dagger \left(\ddot{\mathbf{x}}_\mathbf{d} - \dot{J}_p \dot{\mathbf{q}}_\mathbf{d} \right) \tag{4.16}$$

where ${J_p}^\dagger = \left({J_p}^T J_p \right)^{-1} J_p$. Note, that the equations (4.15) and (4.16) can also be computed through SVD or recursive methods like least squares or damped least squares, and appropriate method should be employed based upon specific case.

After the desired joint space positions $\mathbf{q}_\mathbf{d}$, desired joint space velocities $\dot{\mathbf{q}}_\mathbf{d}$ and the desired joint space acceleration $\ddot{\mathbf{q}}$ are computed, it is possible to implement control methods on the mechanism. The control method used in this work is known as computed torque control. Since, a bipedal robot is an under-actuated system, with more degrees of freedom and less number of actuator torque (more number of state variables compared to the number of inputs in the plant), it is not possible to use

the tracking errors directly to determine the control input for the plant. An inverse dynamics computation needs to be performed on the state variable to generate the actuator torques, which can then be used as the control input to the system.

In the computed torque control system consists of two components: (1) an inner feedforward subsystem and (2) a feedback outer loop [30]. In this work a Proportional-Derivative controller is used for computing the torques inputs to the system. The inner feedforward subsystem takes an input of the error in joint space accelerations and generates actuator torques. Whereas the outer feedback loop computes the error in joint space accelerations based on the position and velocity tracking errors. The position and velocity tracking errors in the system are given by,

$$\mathbf{e} = \mathbf{q_d} - \mathbf{q} \tag{4.17}$$

and,

$$\dot{\mathbf{e}} = \dot{\mathbf{q}}_\mathbf{d} - \dot{\mathbf{q}} \tag{4.18}$$

Then, a proportional-derivative (PD) control law for the outer feedback loop can be written for the system,

$$\mathbf{u} = -K_v\dot{\mathbf{e}} - K_p e \tag{4.19}$$

Where $K_v = diag\{kv_i\}$ and $K_p = diag\{kp_i\}$ are the diagonal matrices containing the derivative kv_i, and the proportional gains kp_i respectively, corresponding to each degree of freedom. In order to have a critically damped system the control gains can be selected such that,

$$kv_i = 2\sqrt{kp_i} \tag{4.20}$$

The error between the outer loop feedback input u and the desired joint space accelerations $\ddot{\mathbf{q}}_\mathbf{d}$, is then used as an input to the inner feedforward subsystem. Thus,

the feedforward subsystem generates the actuator torques, that are used as control inputs to the plant,

$$\Gamma = \left(G^T\right)^{-1} \left[A \left(\ddot{\mathbf{q}}_\mathbf{d} - \mathbf{u}\right) + \mathbf{b}(\mathbf{q}, \dot{\mathbf{q}}) + \mathbf{g}(\mathbf{q})\right] \tag{4.21}$$

Expanding this gives us,

$$\Gamma = \left(G^T\right)^{-1} \left[A \left(\ddot{\mathbf{q}}_\mathbf{d} + K_v\dot{\mathbf{e}} + K_p\mathbf{e}\right) + \mathbf{b}(\mathbf{q}, \dot{\mathbf{q}}) + \mathbf{g}(\mathbf{q})\right] \tag{4.22}$$

CHAPTER 5

SIMULATION RESULTS: ATLAS ROBOT

At this point, all the key elements of this work have been discussed in the preceding chapters. In this chapter, results are presented for the simulation of the bipedal robot, Atlas. In this simulation, the feet of the robot are considered to be undergoing impacts during the walking task. The impacts between the feet and the ground are analyzed using the methods discussed in chapter 2. The actuator torques for the robot model are generated using position and velocity feedback with the help of computed torque control method, as discussed in chapter 4. Figure 5 shows the image of the atlas robot model in the simulation environment.

Two cases of the simulation result are presented. The first set of results correspond to the case when four points are considered for impact between the feet and the ground. The impact analysis would be determinate when four points are considered, this is because the number of degrees of freedom for the robot(in this case its

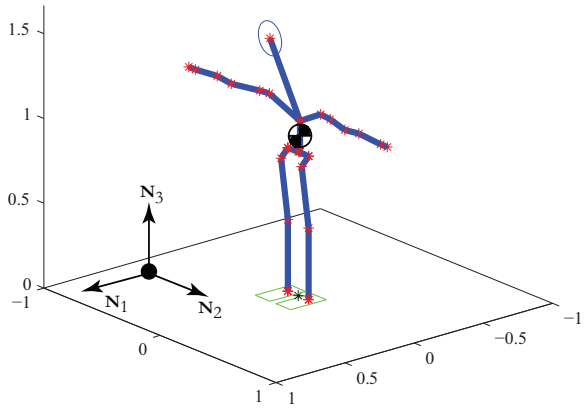

Figure 5.1. Robot Standing in Simulation.

34) would exceed the number of ground constraint forces being considered with four points of contact in either foot. The second result however, would be for an indeterminate situation where eight different contact points are being considered, where the number of ground constraint forces exceed the number of degrees of freedom available to solve for the impulses.

The figure 5.2(a) and 5.2(b) show the motion capture of the walking simulation of the Atlas robot with four point and eight point impact analysis. Figure 5.3 shows the motion capture for the four point and eight point cases from the front and side view. Looking at these images it becomes evident that there is no observable difference in the gait of the robot, as a result of selecting different number of points for analyzing the impacts.

Since the robot model undergoes a large number of impacts during the walking task, it only a few representative impacts are being shown and discussed in this thesis. In the case of walking, whenever a foot of the robot comes into contact with the ground, a series of impact occurs before the foot settles down to a stable contact. Figure 5.4 shows the velocity plots of the left foot of the robot as it takes the first step. In the figure the velocity plots are compared between the four-point and the eight point case. As it was observed in the case of the block in chapter 3, there doesn't seem to be much difference in the velocity plots between the two cases. Note that the normal velocity, shown in magenta, and the sliding velocity, shown in blue, are hovering around zero value, and this could be explained based on the trajectory generation algorithm as explained in chapter 4. Due to the time based cubic spline trajectories, the horizontal component of the desired velocity of the foot control point becomes close to zero as the robot finishes a step. Also, since the vertical component of the desired position is parameterized using the horizontal component, that becomes zero as well. As a result of this, both the normal velocity and the sliding velocities

are close to zero at the beginning of the impact, and only changes slightly before a new impact event takes place. Figure 5.5 shows the normal work during the impact event. Again, we notice a lot of similarity between the four and eight point cases. Note for the first impact, in the four point case the end of restitution phase work is slightly above -4×10^{-5} and also for the eight point case the restitution phase ends at slightly above -4×10^{-5}, which shows that similar amount of energy loss is occurring in both the cases. Therefore, based on the results of this chapter and chapter 3, it can be concluded that the increasing the number of points for analysis on the feet of legged robotic system doesn't change the overall post-impact behavior of the legged system in a simulation environment. This result, as stated before, can enable us to completely ignore the additional analysis required for appropriate placement of the points on the surface for analysis, as a large number of evenly distributed points could be analyzed using the methods discussed in this work.

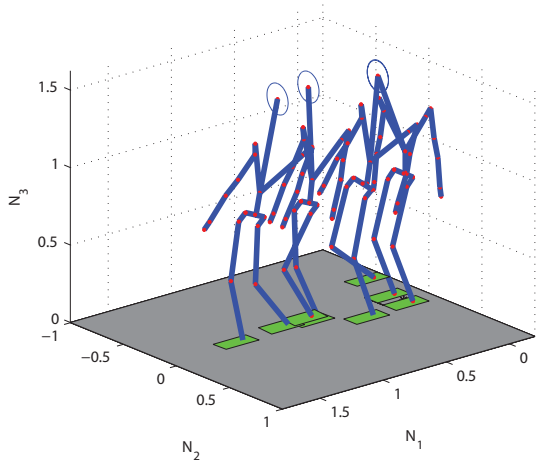

(a) Four-Point Analysis per Foot

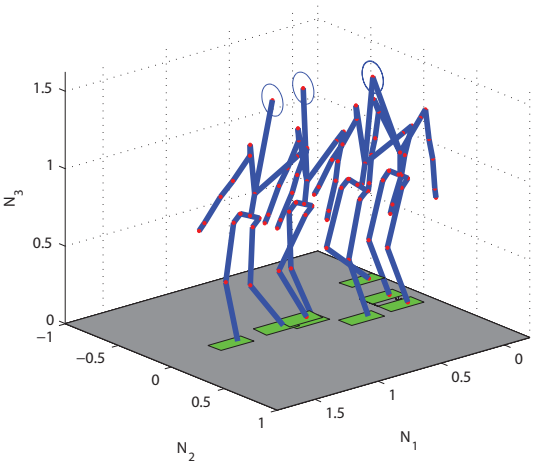

(b) Eight-Point Analysis per Foot

Figure 5.2. Motion Capture of the Atlas Robot Performing a Walking Task.

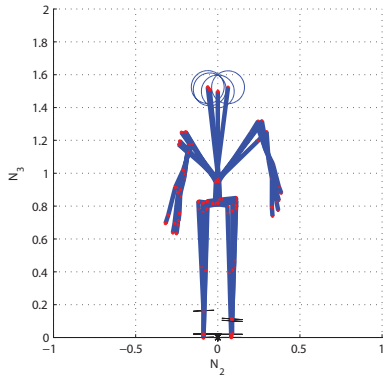

(a) Four-Point Analysis per Foot

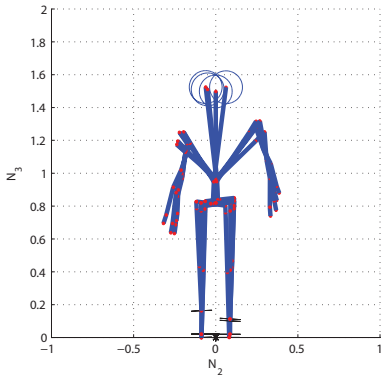

(b) Eight-Point Analysis per Foot

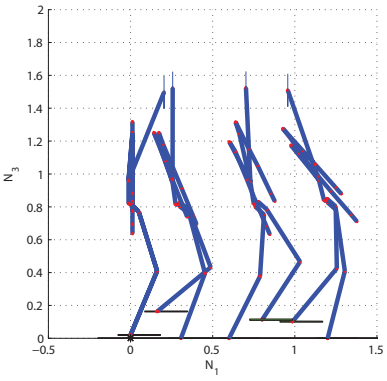

(c) Four-Point Analysis per Foot

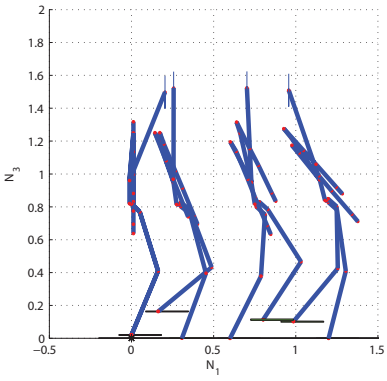

(d) Eight-Point Analysis per Foot

Figure 5.3. Front and Side View of Atlas Robot while Performing a Walking Task.

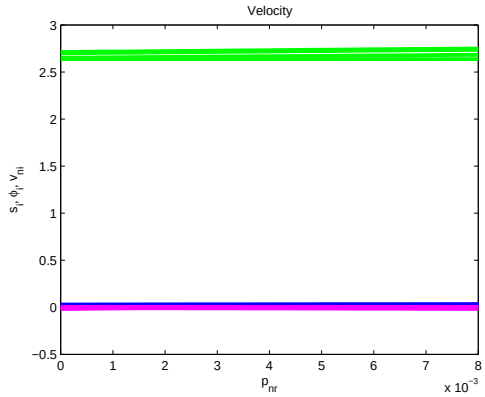

(a) First Four-Point Impact Velocity Plot

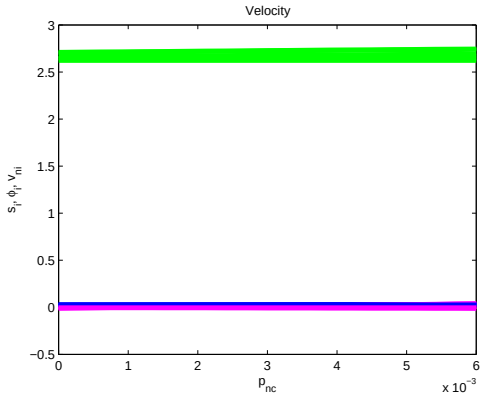

(b) First Eight-Point Impact Velocity Plot

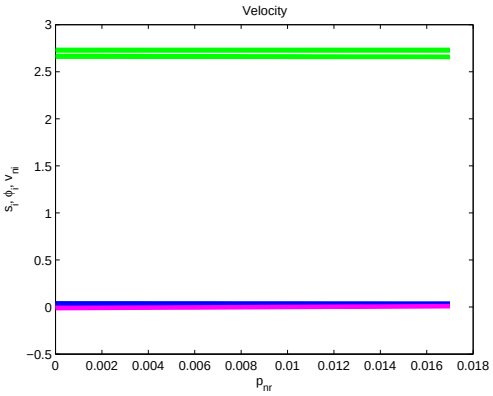

(c) Second Four-Point Impact Velocity Plot

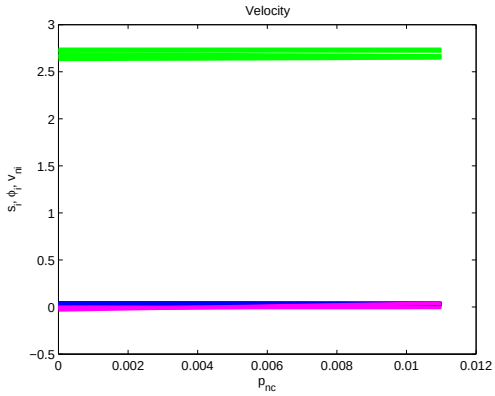

(d) Second Eight-Point Impact Velocity Plot

Figure 5.4. Feet Velocities during Impact.

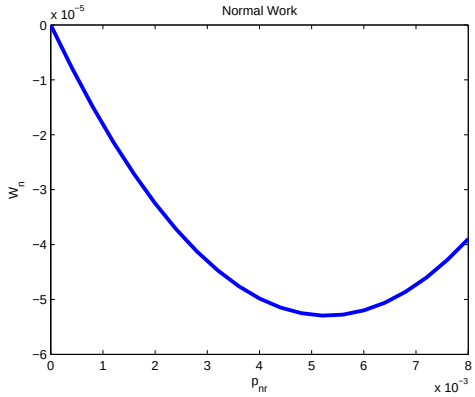

(a) First Four-Point Impact Normal Work Plot

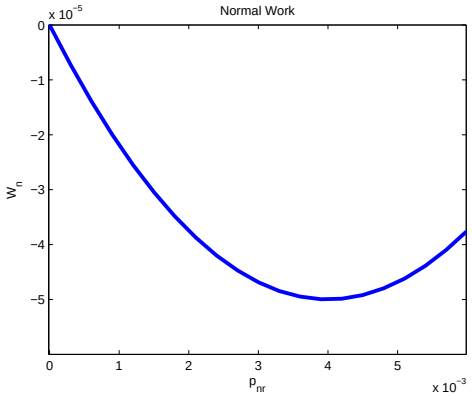

(b) First Eight-Point Impact Normal Work Plot

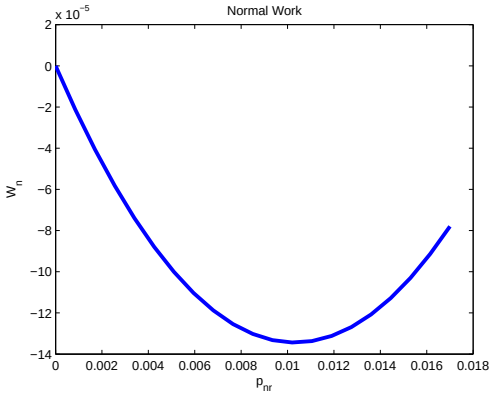

(c) Second Four-Point Impact Normal Work Plot

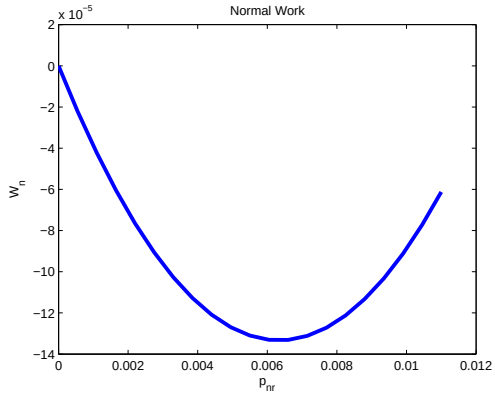

(d) First Eight-Point Impact Normal Work Plot

Figure 5.5. Feet Normal Work during Impact.

APPENDIX A

RIGID BODY CONSTRAINT USING VELOCITY-PROJECTION METHOD

In order to demonstrate the procedure for deriving the rigid body constraints, lets consider the example of two impacting points, which are denoted as A and B, in this case. The velocity constraint equation that can be obtained by setting the relative velocities of the points A and B, can be written as,

$$(v_{t1A} - v_{t1B}) + (v_{t2A} - v_{t2B})\alpha + \ (v_{nA} - v_{nB})\beta = \ 0 \tag{A.1}$$

where, α and β are the direction cosines of the points A and B. Then the velocity vector can be rewritten as,

$$\boldsymbol{\vartheta} \ = \begin{bmatrix} v_{t1B} - (v_{t2A} - v_{t2B})\alpha - (v_{nA} - v_{nB})\beta \\ v_{t2A} \\ v_{nA} \\ v_{t1B} \\ v_{t2B} \\ v_{nB} \\ v_{t1C} \\ v_{t2C} \\ v_{nC} \\ v_{t1D} \\ v_{t2D} \\ v_{nD} \end{bmatrix} = Q\boldsymbol{\vartheta}^* \tag{A.2}$$

where,

$$Q = \begin{bmatrix} -\alpha & -\beta & 1 & \alpha & \beta & 0 & 0 & 0 & 0 & 0 & 0 \\ 1 & 0 & 0 & 0 & 0 & 0 & 0 & 0 & 0 & 0 & 0 \\ 0 & 1 & 0 & 0 & 0 & 0 & 0 & 0 & 0 & 0 & 0 \\ 0 & 0 & 1 & 0 & 0 & 0 & 0 & 0 & 0 & 0 & 0 \\ 0 & 0 & 0 & 1 & 0 & 0 & 0 & 0 & 0 & 0 & 0 \\ 0 & 0 & 0 & 0 & 1 & 0 & 0 & 0 & 0 & 0 & 0 \\ 0 & 0 & 0 & 0 & 0 & 1 & 0 & 0 & 0 & 0 & 0 \\ 0 & 0 & 0 & 0 & 0 & 0 & 1 & 0 & 0 & 0 & 0 \\ 0 & 0 & 0 & 0 & 0 & 0 & 0 & 1 & 0 & 0 & 0 \\ 0 & 0 & 0 & 0 & 0 & 0 & 0 & 0 & 1 & 0 & 0 \\ 0 & 0 & 0 & 0 & 0 & 0 & 0 & 0 & 0 & 1 & 0 \\ 0 & 0 & 0 & 0 & 0 & 0 & 0 & 0 & 0 & 0 & 1 \end{bmatrix}$$

and

$$\boldsymbol{\vartheta}^* = \begin{bmatrix} v_{t2A} & v_{nA} & v_{t1B} & v_{t2B} & v_{nB} & v_{t1C} & v_{t2C} & v_{nC} & v_{t1D} & v_{t2D} & v_{nD} \end{bmatrix}^T$$

The Q matrix contains all the velocity constraints and $\boldsymbol{\vartheta}^*$ contains the independent velocities. The dual nature of the jacobian expresses relationships between velocities as well as forces. Therefore, the constraint matrix can be used along with the jacobian matrix to derive constraint relationships between the impact forces,

$$\boldsymbol{\vartheta}^* = Q^+ \boldsymbol{\vartheta} = Q^+ J \dot{\mathbf{q}} \tag{A.3}$$

and,

$$\boldsymbol{\Gamma} = J^T \mathbf{F} = J^T (Q^+)^T \mathbf{F}^* \tag{A.4}$$

where $Q^+ = (Q^T Q)^{-1} Q^T$ is the left-inverse of Q, and $\mathbf{F}^*$ is a vector containing all the independent impact forces. Expression (A.4) further yields,

$$\mathbf{F} = (Q^+)^T \mathbf{F}^* \qquad\qquad \mathbf{F}^* = Q^T \mathbf{F} \tag{A.5}$$

Using (A.5), $\mathbf{F}^*$ is first computed using Q^T,

$$\mathbf{F}^* = Q^T\mathbf{F} = \begin{bmatrix} -\alpha f_{t1\ A} + f_{t2\ A} \\ -\beta f_{t1\ A} + f_{n\ A} \\ f_{t1\ A} + f_{t1\ B} \\ \alpha f_{t1\ A} + f_{t2\ B} \\ \beta f_{t1\ A} + f_{nB} \\ f_{t1\ C} \\ f_{t2\ C} \\ f_{nC} \\ f_{t1\ D} \\ f_{t2\ D} \\ f_{nD} \end{bmatrix} \tag{A.6}$$

Next, the vector $\mathbf{F}^*$, derived in (A.6), would be used derive the constraint equations for the impact forces. The following step was performed with the help of a symbolic computation software, due to its lengthy and tedious nature.

$$\mathbf{F} - (Q^+)^T\mathbf{F}^* = 0 \tag{A.7}$$

Yields,

$$\begin{bmatrix} f_{t1\,A} - f_{t1\,B} + \alpha f_{t2\,A} - \alpha f_{t2\,B} + \beta f_{n\,A} - \beta f_{n\,B} \\ \alpha f_{t1\,A} - \alpha f_{t1\,B} + \alpha^2 f_{t2\,A} - \alpha^2 f_{t2\,B} + \alpha\beta f_{nA} - \alpha\beta f_{n\,B} \\ \alpha f_{t1\,A} - \beta f_{t1\,B} + \alpha\beta f_{t2\,A} - \alpha\beta f_{t2\,B} + \beta^2 f_{nA} - \beta^2 f_{n\,B} \\ -f_{t1\,A} + f_{t1\,B} - \alpha f_{t2\,A} + \alpha f_{t2\,B} - \beta f_{n\,A} + \beta f_{n\,B} \\ -\alpha f_{t1\,A} + \alpha f_{t1\,B} - \alpha^2 f_{t2\,A} + \alpha^2 f_{t2\,B} - \alpha\beta f_{nA} + \alpha\beta f_{n\,B} \\ -\beta f_{t1\,A} + \beta f_{t1\,B} - \alpha\beta f_{t2\,A} + \alpha\beta f_{t2\,B} - \beta^2 f_{nA} + \beta^2 f_{n\,B} \\ 0 \\ 0 \\ 0 \end{bmatrix} = \begin{bmatrix} 0 \\ 0 \\ 0 \\ 0 \\ 0 \\ 0 \\ 0 \\ 0 \\ 0 \end{bmatrix}$$

The first equation among these can be rewritten as,

$$f_{t1\,A} - f_{t1\,B} + \alpha(f_{t2\,A} - f_{t2\,B}) + \beta(f_{n\,A} - f_{n\,B}) = 0 \tag{A.8}$$

Multiplying both sides with an infinitesimal small time interval dt, converts the whole equation in terms of impulses, thus essentially describing the velocity based rigid body constraint equations in terms of impulses,

$$(dp_{t1\,A} - dp_{t1\,B}) + (dp_{t2\,A} - dp_{t2\,B})\alpha + (dp_{n\,A} - dp_{n\,B})\beta = 0 \tag{A.9}$$

APPENDIX B

SIMULATION TECHNIQUE

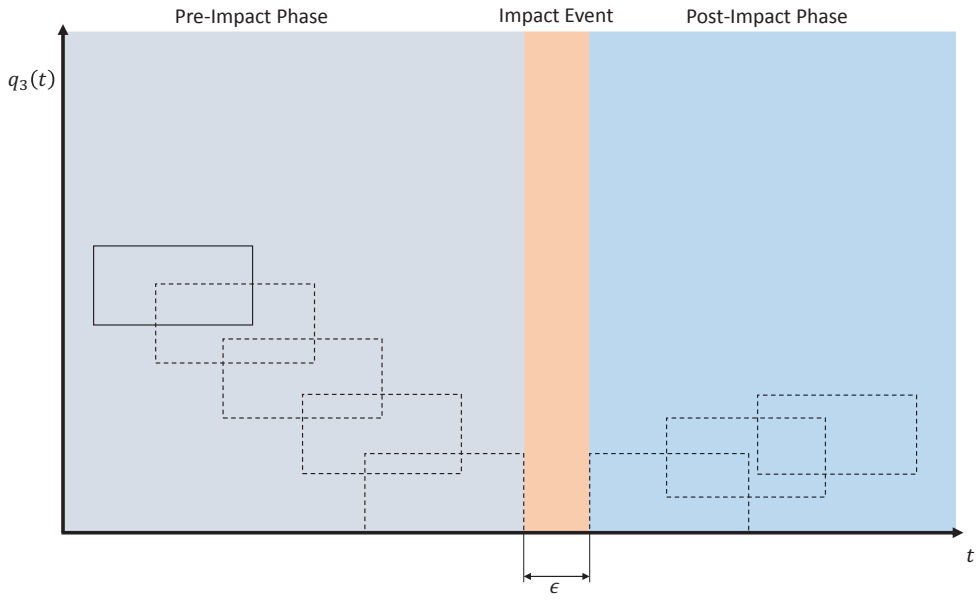

Figure B.1. Event Based Approach.

The simulation technique discussed in this section are based on the example problem of three-dimensional block without any loss of generality, and thus could also be implemented in a full model of a legged robot. The entire simulation can be divided into three phases: pre-impact simulation, impact-event simulation, and post-impact simulation. The pre- and post-impact simulation are the simulations of the same equations of motion of the block or robot without the contact constraint forces (or with $\mathbf{F}$ set as a zero vector). The difference between the pre- and the post-impact simulation arise due to the different initial conditions considered for each. The impact-event simulation is based on the method presented thus far in this paper. The simulation begins by setting up the equations of motion without the forcing terms in a numerical integrator with some desired initial conditions. For this research, an open source C++ function called *rkevent*, which is based on the Kutta-Merson Algorithm, was used as an integrator and numerical derivative values based on the equations

of motion was generated with the help of *Rigid Body Dynamics Library*, which is based on Roy Featherstone's multibody dynamics algorithm [32]. The simulation is stopped as soon as an impact with the ground is detected, which also marks the end of pre-impact simulation. The $\dot{\mathbf{q}}$ at end of the pre-impact and the jacobian for the impacting point(s), are used to calculate the Cartesian space velocities, which are subsequently transformed into cylindrical coordinates and used as initial conditions for (2.20). Another numerical integration is performed to simulate (2.20). Conditions for the stick-slip transition is checked at every integration step during the integration. If any of the impact point reaches the stick-slip transition, $\bar{\mu}_j$ is evaluated using (2.26). $\bar{\mu}_j$ is compared with μ_j to determine whether the point sticks or slip-reverses, using the relation stated in (2.26). If the point slip-reverses, then the sliding direction becomes constant and unique as in (2.27). The μ_j is replaced by $\bar{\mu}_j$ in the entire evaluation of (2.20) if the point is in stick-slip transition.

The normal work, W_n as given in, (2.30) is calculated along with the velocities using the numerical integrator. W_{nc}, which corresponds to the work at the end of the compression phase, can be determined by finding the minimum normal work. After W_{nc} is determined, W_{nf}, which is the work at the end of restitution phase or impact, is calculated using Stronge's energetic coefficient of restitution(ECOR), as shown in (2.33). The simulation is stopped when Wn reaches W_{nf},which marks the end of an impact event. At the end of the impact-event the normal component of the post-impact velocities are checked. If any of the normal velocity components is/are negative, the points corresponding to those normal velocities proceed for another impact event in which the entire procedure is repeated using those points. If none of the normal velocities are negative at the end of the impact-event phase, the simulation proceeds to the post-impact phase. In the post-impact phase, the post-impact velocities, obtained at the end of the impact event, are used with the inverse of the

Jacobian matrix to transform the post impact velocities in terms of the generalized coordinates, $\dot{\mathbf{q}}$. Finally, the unforced equations of motion is numerically integrated using the post-impact velocities (in terms of generalized coordinates) as the initial condition.

REFERENCES

[1] A. Rodriguez, "Dynamic simulation of multibody systems in simultaneous, indeterminate contact and impact with friction," Ph.D. dissertation, UNIVERSITY OF TEXAS AT ARLINGTON, 2014.

[2] Y.-T. Wang, V. Kumar, and J. Abel, "Dynamics of rigid bodies undergoing multiple frictional contacts," in *Robotics and Automation, 1992. Proceedings., 1992 IEEE International Conference on*. IEEE, 1992, pp. 2764–2769.

[3] Y.-B. Jia, "Energy-based modeling of tangential compliance in 3-dimensional impact," in *Algorithmic Foundations of Robotics IX*. Springer, 2011, pp. 267–284.

[4] P. R. Kraus and V. Kumar, "Compliant contact models for rigid body collisions," in *Robotics and Automation, 1997. Proceedings., 1997 IEEE International Conference on*, vol. 2. IEEE, 1997, pp. 1382–1387.

[5] G. Darboux, "Etude géométrique sur les percussions et le choc des corps," *In Bulletin des Sciences Mathématiques et Astronomiques, deuxiéme série*, vol. 4, no. 1, pp. 126–160, 1880.

[6] E. Whittaker, *A Treatise on the Analytical Dynamics of Particles and Rigid Bodies*. Cambridge University Press, 2nd ed., 1917.

[7] J. Keller, "Impact with friction," *Journal of Applied Mechanics, Transactions ASME*, vol. 53, no. 1, pp. 1–4, Mar. 1986.

[8] D. M. Flickinger and A. Bowling, "Simultaneous oblique impacts and contacts in multibody systems with friction," *Multibody System Dynamics*, vol. 23, no. 3, pp. 249–261, 2010.

[9] I. Huněk, "On a penalty formulation for contact-impact problems," *Computers & structures*, vol. 48, no. 2, pp. 193–203, 1993.

[10] J. C. Simo and T. Laursen, "An augmented lagrangian treatment of contact problems involving friction," *Computers & Structures*, vol. 42, no. 1, pp. 97–116, 1992.

[11] P. Papadopoulos and J. Solberg, "A lagrange multiplier method for the finite element solution of frictionless contact problems," *Mathematical and computer modelling*, vol. 28, no. 4, pp. 373–384, 1998.

[12] A. Rodriguez and A. Bowling, "Solution to indeterminate multi-point impact with frictional contact using constraints," *Multibody System Dynamics*, vol. 28, no. 4, pp. 313–330, November 2012.

[13] ——, "Study of newton's cradle using a new discrete approach," *Multibody System Dynamics*, 2013, DOI:10.1007/s11044-013-9406-3.

[14] ——, "Analytic solution of indeterminate multi-point impact problems using stronge's hypothesis," *Multibody System Dynamics*, 2014, (under review).

[15] W. Stronge, *Impact Mechanics*. Cambridge University Press, 2000.

[16] S. Djerassi, "Three-dimensional, one point collision with friction," *Multibody System Dynamics*, vol. 27, no. 2, pp. 173–195, Feb. 2012.

[17] V. Bhatt and J. Koechling, "Three-dimensional frictional rigid-body impact," *Journal of Applied Mechanics*, vol. 62, no. 4, pp. 893–898, Dec. 1995.

[18] ——, "Partitioning the parameter space according to different behaviors during three-dimensional impacts," *ASME Journal of Applied Mechanics*, vol. 62, no. 3, pp. 740–746, Sept. 1995.

[19] D. Marghitu and Y. Hurmuzlu, "Three-dimensional rigid-body collisions with multiple contact points," *ASME Journal of Applied Mechanics*, vol. 62, no. 3, pp. 725–732, Sept. 1995.

[20] R. Brach, *Mechanical Impact Dynamics*. Wiley, New York, 1991.

[21] V. Bhatt and J. Koechling, "Classifying dynamic behavior during three dimensional frictional rigid body impact," in *Robotics and Automation, 1994. Proceedings., 1994 IEEE International Conference on*. IEEE, 1994, pp. 2342–2348.

[22] P. Bergés and A. Bowling, "Rebound, slip, and compliance in the modeling and analysis of discrete impacts in legged locomotion," *Journal of Vibration and Control*, vol. 17, no. 12, pp. 1407–1430, Dec. 2006.

[23] J. Moreau, "Numerical aspects of the sweeping process," *Computer Methods in Applied Mechanics and Engineering*, vol. 177, no. 3, pp. 329–349, May 1999.

[24] J. Batlle, "The sliding velocity flow of rough collisions in multibody systems," *ASME Journal of Applied Mechanics*, vol. 63, no. 3, pp. 804–809, Sept. 1996.

[25] M. Brake, "An analytical elastic-perfectly plastic contact model," *International Journal of Solids and Structures*, vol. 49, no. 22, pp. 3129–3141, Nov. 2012.

[26] R. Jackson, I. Green, and D. Marghitu, "Predicting the coefficient of restitution of impacting elastic-perfectly plastic spheres," *Nonlinear Dynamics*, vol. 60, no. 3, pp. 217–229, Mar. 2010.

[27] S. R. Buss, "Introduction to inverse kinematics with jacobian transpose, pseudoinverse and damped least squares methods," *IEEE Journal of Robotics and Automation*, vol. 17, pp. 1–19, 2004.

[28] C. W. Wampler, "Manipulator inverse kinematic solutions based on vector formulations and damped least-squares methods," *Systems, Man and Cybernetics, IEEE Transactions on*, vol. 16, no. 1, pp. 93–101, 1986.

[29] Y. Nakamura and H. Hanafusa, "Inverse kinematic solutions with singularity robustness for robot manipulator control," *Journal of dynamic systems, measurement, and control*, vol. 108, no. 3, pp. 163–171, 1986.

[30] F. L. Lewis, D. M. Dawson, and C. T. Abdallah, *Robot manipulator control: theory and practice*. CRC Press, 2003.

[31] J. J. Craig, *Introduction to robotics: mechanics and control*. Pearson Prentice Hall Upper Saddle River, 2005, vol. 3.

[32] R. Featherstone, *Rigid body dynamics algorithms*. Springer, 2014.

BIOGRAPHICAL STATEMENT

Abhishek Chatterjee was born in Calcutta (now Kolkata), India, in 1990. He came to the United States in 2009 to pursue higher education. He received his B.S. degree from Midwestern State University in 2013, before joining The University of Texas at Arlington for graduate studies in Mechanical Engineering. His research interest is in the area of robotic manipulation and controls, and wishes to continue working on these areas, as a PhD student.